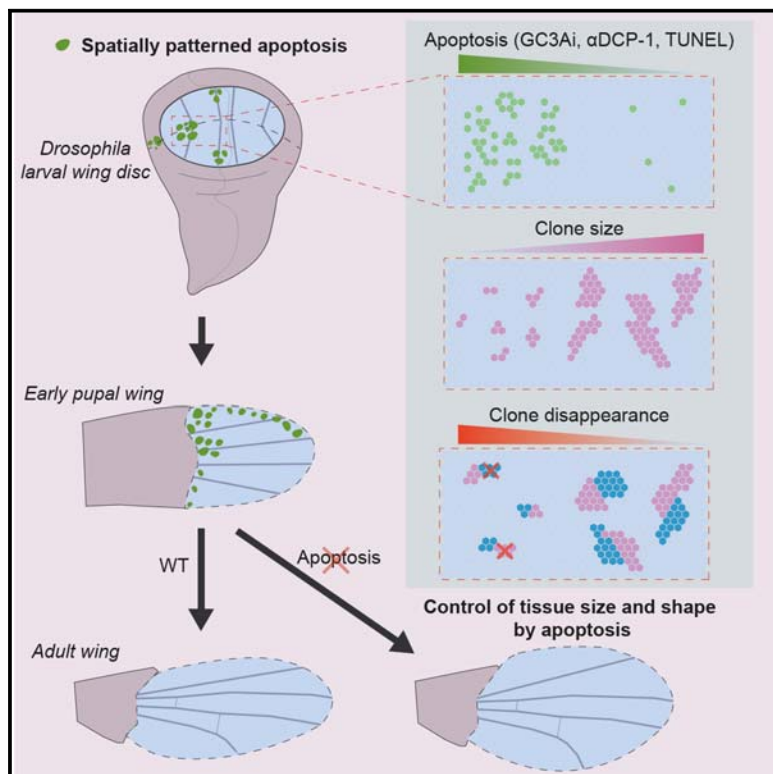


### Patterned apoptosis has an instructive role for local growth and tissue shape regulation in a fast-growing epithelium

#### Graphical abstract



#### Authors

Alexis Matamoro-Vidal,  
Tom Cumming, Andela Davidović,  
Florence Levillayer, Romain Levayer

#### Correspondence

romain.levayer@pasteur.fr

#### In brief

Matamoro-Vidal et al. use systematic and quantitative characterization of apoptosis in the *Drosophila* wing imaginal disc and pupal wing to reveal stereotyped spatial patterns of apoptosis that locally reduce growth, increase the probability of clone disappearance, and modulate adult wing shape and size.

#### Highlights

- Hotspots of apoptosis are present in *Drosophila* wing discs and pupal wings
- These hotspots reduce net growth and increase clone disappearance locally
- Patterned apoptosis has a significant impact on adult wing size and shape
- Apoptosis fine-tunes organ shape and size even in the context of growth



Article

# Patterned apoptosis has an instructive role for local growth and tissue shape regulation in a fast-growing epithelium

Alexis Matamoro-Vidal,<sup>1</sup> Tom Cumming,<sup>1,2</sup> Andela Davidović,<sup>3</sup> Florence Levillayer,<sup>1</sup> and Romain Levayer<sup>1,4,5,\*</sup>

<sup>1</sup>Department of Developmental and Stem Cell Biology, Institut Pasteur, CNRS UMR 3738, Université Paris Cité, Cell Death and Epithelial Homeostasis Unit, 75015 Paris, France

<sup>2</sup>PPU program Institut Pasteur, Sorbonne Université, Collège Doctoral, 75005 Paris, France

<sup>3</sup>Institut Pasteur, Université Paris Cité, Bioinformatics and Biostatistics Hub, 75015 Paris, France

<sup>4</sup>X (formerly Twitter): [@LevayerR](#)

<sup>5</sup>Lead contact

\*Correspondence: [romain.levayer@pasteur.fr](mailto:romain.levayer@pasteur.fr)

<https://doi.org/10.1016/j.cub.2023.12.031>

## SUMMARY

What regulates organ size and shape remains one fundamental mystery of modern biology. Research in this area has primarily focused on deciphering the regulation in time and space of growth and cell division, while the contribution of cell death has been overall neglected. This includes studies of the *Drosophila* wing, one of the best-characterized systems for the study of growth and patterning, undergoing massive growth during larval stage and important morphogenetic remodeling during pupal stage. So far, it has been assumed that cell death was relatively neglectable in this tissue both during larval stage and pupal stage, and as a result, the pattern of growth was usually attributed to the distribution of cell division. Here, using systematic mapping and registration combined with quantitative assessment of clone size and disappearance as well as live imaging, we outline a persistent pattern of cell death and clone elimination emerging in the larval wing disc and persisting during pupal wing morphogenesis. Local variation of cell death is associated with local variation of clone size, pointing to an impact of cell death on local growth that is not fully compensated by proliferation. Using morphometric analyses of adult wing shape and genetic perturbations, we provide evidence that patterned death locally and globally affects adult wing shape and size. This study describes a roadmap for precise assessment of the contribution of cell death to tissue shape and outlines an important instructive role of cell death in modulating quantitatively local growth and morphogenesis of a fast-growing tissue.

## INTRODUCTION

The search of cellular mechanisms underlying variation in organ's size and shape is essential to our understanding of health and evolution. These mechanisms include changes in cell shape, cell proliferation, oriented cell division, oriented cell intercalation, and also cell death.<sup>1</sup> Programmed cell death and apoptosis are indeed essential regulators of development and morphogenesis.<sup>2</sup> For instance, cell death is required to eliminate scaffolding tissues, which are not present in the adult body. Apoptosis in epithelia is also a driving force of morphogenesis, which can help to fuse tissues by generating pulling forces<sup>3</sup> or trigger fold formations by generating apico-basal traction forces.<sup>4,5</sup> Finally, apoptosis has been associated with the buffering of developmental fluctuations, which can eliminate miss-specified/miss-patterned cells through cell competition,<sup>6</sup> morphogenetic apoptosis,<sup>7,8</sup> cell sorting and extrusion,<sup>9–11</sup> or more recently, with the buffering of mismatch between the size of the tissue and the shape of morphogen gradients.<sup>12</sup> Interestingly, while the functions of apoptosis are numerous, its contribution to the

regulation of organ size and growth, especially in tissues undergoing fast expansion, has been poorly studied. Accordingly, emphasis has mostly been given to cellular growth regulation including the increase of cell volume and cell proliferation.<sup>13–21</sup> Moreover, systematic and quantitative evaluations of the pattern and number of cell deaths remain relatively rare and tedious, especially in tissues that are not appropriate for long-term live imaging.<sup>22–24</sup> Thus, the exact pattern of cell death and its real contribution to the regulation of organ size and shape remain poorly documented in many situations. This also applies to the *Drosophila* wing, one of the best-studied systems for understanding patterning and growth regulation.<sup>15,17,25–28</sup>

*Drosophila* wing development can be separated in the larval stage, where the wing imaginal disc mostly undergoes massive proliferation and patterning, followed by the pupal stage, where complex morphogenetic movements give rise to the final wing shape.<sup>29</sup> At larval stages, *Drosophila* wing imaginal discs are epithelial sacs composed of two epithelia: the peripodial cells (squamous epithelium) and a pseudostratified epithelium that will form the adult structures.<sup>30</sup> The disc is separated into a distal



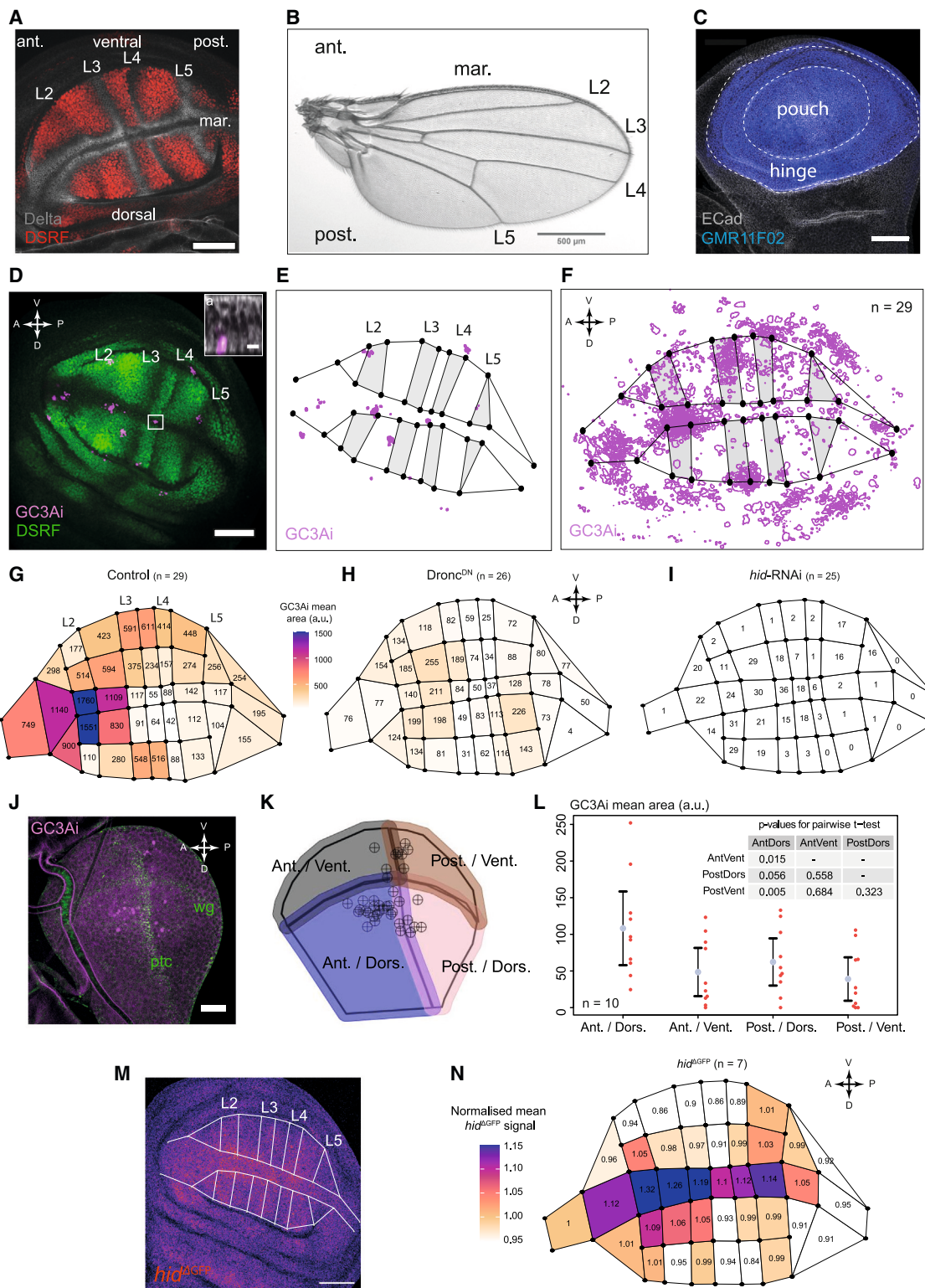


**Figure 1. Apoptosis is spatially biased in the developing wing tissue**

(A) Wing disc at ~96 h after egg laying (AEL) showing veins (L2 to L5), interveins (red), dorsal, ventral, margin (mar.), anterior (ant.), and posterior (post.) territories. Red: anti-DSRF immunostaining. Gray: anti-Delta immunostaining. Orientation is the same for all wing discs images and schemes of this article, with the anterior compartment leftward and the dorsal compartment downward.

(B) Female adult wing on dorsal view, with longitudinal veins (L2 to L5), margin (mar.), anterior (ant.), and posterior (post.) territories.

domain that will give rise to the adult wing blade (the wing pouch or wing proper) and a proximal region called the hinge that will connect the wing to the thorax. This wing pouch is patterned in different domains prefiguring adult wing structures: the pro-vein domains L2 to L5 and the dorsal-ventral boundary that will give rise, respectively, to the adult wing veins and the adult wing boundaries (Figures 1A and 1B). Wing imaginal discs undergo massive growth during larval development through several rounds of cell division (9 to 11 cycles).<sup>31,32</sup> This growth phase is followed by profound remodeling and morphogenesis during the pupal stage,<sup>33</sup> including wing eversion and apposition of the dorsal and ventral epithelial layers,<sup>34,35</sup> the elongation of the wing proper through distal anchoring and hinge contraction,<sup>27,36</sup> global tissue growth by cell expansion, and folding<sup>37</sup> eventually followed by hatching and wing spreading<sup>38</sup> (Figures 1A and 1B). All these steps are performed with a high degree of precision and reproducibility, leading to an extremely reproducible shape, especially comparing intra-individual left and right wings.<sup>39</sup>

Decades of work sought to dissect the mechanisms controlling the growth and size of the *Drosophila* wing, and these have mostly focused on the distribution and regulation of cell proliferation while neglecting cell death.<sup>15–19,21</sup> Indeed, seminal works more than 20 years ago found that cell death is relatively minor in the wing disc and that it occurs sporadically without any noticeable pattern.<sup>23</sup> Similarly, recent systematic tracking of cells in the pupal wing during elongation (between 16 and 32 h after pupal formation [APF]) suggested that apoptosis has also a minor role in wing elongation at the pupal stage.<sup>27,40</sup> Yet, these works did not exclude more subtle functions of cell death.

Accordingly, apoptosis was proposed to buffer developmental fluctuations to ensure reproducible wing size.<sup>41</sup> This was assumed to be based on cell competition—the context-dependent elimination of suboptimal cells from growing tissues.<sup>42,43</sup> Interestingly, although the studies of cell competition are mostly based on the analysis of mutant clone disappearance in the wing disc, we know very little about spontaneous clone

disappearance during normal wing development and the prevalence, localization, and functions of physiological cell competition. Recently, apoptosis was proposed to fine-tune Decapentaplegic (Dpp) gradient shape by eliminating supernumerary cells to match gradient decay length and tissue size.<sup>12</sup> Alternatively, basal sublethal effector caspase activity was also proposed to modulate global wing growth and size.<sup>44</sup> These results call for a reassessment and more thorough characterization of cell death in the wing and its contribution to growth and tissue shape.

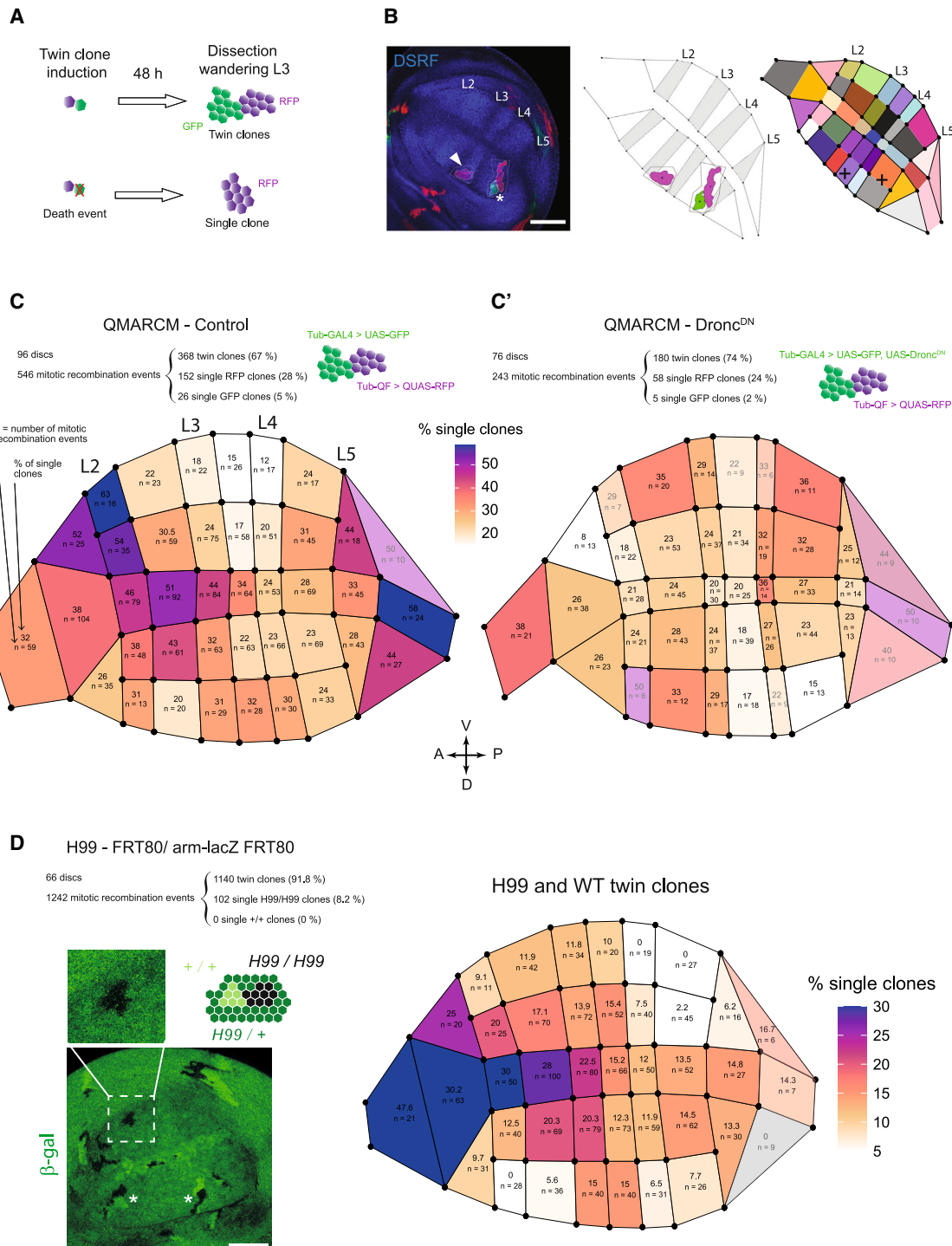
Here, we performed systematic mapping of apoptosis, using various markers of caspases and apoptosis, together with spatial registration in the larval wing imaginal disc. Unexpectedly, we found striking reproducible biases in the distribution of cell death, which outlined hotspots of apoptosis. These hotspots correlate with a local increase of clone disappearance probability and significantly reduce local net growth in the wing disc. Using live imaging of the pupal wing, we also showed that these spatial biases persist at early pupal development and that new spots of apoptosis appear later during development. Finally, using morphometric analysis, we further demonstrate that these hotspots can tune adult wing size and shape. Altogether, we reveal that apoptosis cannot be neglected for the study of growth/size and is also an essential modulator of local shape and growth, even in a fast-expanding tissue. Our study also proposes a roadmap for a more systematic characterization of the contribution of cell death to clone dynamics and tissue growth.

## RESULTS

### Caspase activity and apoptosis are spatially biased in the larval wing pouch

We first systematically evaluated the distribution of apoptotic cells in the *Drosophila* wing disc at the larval wandering stage (96 h after egg laying [AEL]). We used the live effector caspase reporter GC3Ai<sup>45</sup> driven in the larval pouch and hinge by the driver GMR11F02-GAL4 (Figure 1C). The brightest GFP spots revealed by the reporter correspond to cell debris located on the

- (C) Wing disc at ~96 h AEL showing the GMR11F02-GAL4 expression domain (blue, UAS-RFP). Gray: anti E-Cad.
- (D) z projection of a wing disc showing caspase-3 activity using the GC3Ai reporter (magenta), expressed under the control of GMR11F02-GAL4 at ~96 h AEL. Inset: orthogonal view of the white square, showing that the GC3Ai signal (magenta) points to apoptotic bodies located basally in the epithelium. a: apical. Gray: E-cadherin. Inset scale bars: 5  $\mu$ m.
- (E) Segmentation output from the disc in (D), showing the DSRF pattern and the GC3Ai segmented signal (magenta). Veins regions are gray.
- (F) Superimposition of the segmentation data from 29 discs scaled, rotated, and aligned using the general Procrustes analysis (GPA), showing a spatially heterogeneous signal for GC3Ai (magenta). The map shown for vein/intervein territories is the average map from the 29 discs.
- (G–I) Heatmaps showing the average GC3Ai-positive area on each of the 40 compartments of the wing disc for the *control* (G, n = 29), *Dronc*<sup>DN</sup> (H, n = 26), and *hid*-*RNAi* (I, n = 25) genotypes. Numbers within each compartment show the average value for GC3Ai-positive area (arbitrary units), also shown as a color-coded heatmap, same scale for three maps.
- (J) Visualization of caspase-3 activity using the GC3Ai reporter (magenta), expressed under the control of GMR11F02-GAL4 at ~72 h AEL. The wing disc is divided into four quadrants (anterior-dorsal, anterior-ventral, posterior-dorsal, and posterior-ventral) using the immunostaining anti-Wingless (Wg) and anti-Patched (Ptc) marking compartment boundaries (green).
- (K) Segmentation of the disc shown in (J). The circled black crosses are centroids of the segmented GC3Ai signal. The black line was manually drawn using anti-Wingless and anti-Patched immunostainings to delineate the four quadrants, which are colored (including overlapping of quadrant to count uncertainty, see STAR Methods).
- (L) Mean GC3Ai-positive area for 10 discs at ~72 h AEL. One red dot, one disc, blue circles: means, error bars: 95% confidence intervals. Inset: p values for all pairwise t tests between quadrants.
- (M) Pattern of *hid*<sup>ΔGFP</sup> (KI) on a single wing disc (look up table [LUT] fire, Gaussian blur 0.75). White lines: vein/intervein territories extracted from the anti-DSRF immunostaining (not shown).
- (N) Heatmap showing the mean *hid*<sup>ΔGFP</sup> signal on each of the 40 compartments over n = 17 discs. GFP signal intensity was normalized by the average intensity for each disc. All scale bars are 50  $\mu$ m length, except in (B), 500  $\mu$ m, and in (J), 25  $\mu$ m. See also Figure S1.



basal sides, thus staining cells that already extruded (Schott et al.<sup>45</sup>; Figure 1D). We confirmed the accuracy of the GC3Ai marker, as we obtained a similar pattern with cleaved caspase-3 staining (cleaved DCP1), although this was less sensitive and failed to mark the cells with faint GC3Ai signal (Figures S1E–S1G'). Moreover, bright GC3Ai dots used for the analysis co-localized with terminal deoxynucleotidyl transferase dUTP nick end labeling (TUNEL)-positive cells (Figures S1E–S1G'), confirming that they marked late apoptotic cells. To obtain an averaged map of the spatial distribution of cell death, we used spatial landmarks, whose positions were defined by the intervein marker Drosophila serum response factor (DSRF, Figures 1D and 1E). The landmarks positions were used to divide every dissected wing disc into 40 subcompartments (Figures S1A–S1D). In addition, we applied Procrustes transformation (translation, rotation, and scaling) on landmarks' positions to align the discs and superimpose GC3Ai/Dcp1/TUNEL spatial data from many individuals on a single image (see STAR Methods). The averaged distribution of apoptotic cells revealed a striking non-homogeneous distribution of apoptosis with the strongest "hot spot" located in the anterior-dorsal quadrant, near the dorsal-ventral boundary (Figures 1F and 1G,  $p < 0.001$ , Moran autocorrelation spatial test, null hypothesis = homogeneous distribution). This bias is not driven by the Gal4 driver or any side effect of GC3Ai, as a similar pattern was obtained in the  $w^-$  background with cleaved caspase-3 staining (Figures S1H and S1I) or with TUNEL staining (Figures S1J and S1K, Moran's  $p = 0.007$ ). To check whether the spatial bias of GC3Ai signal persists during wing disc development, we also monitored GC3Ai-positive cells in the early L3 wing disc (72 h AEL). As we could not use the same spatial landmarks (the intervein regions are not yet defined at this stage), we instead used the location of the four compartments defined by AP and DV compartment boundaries (anterior, posterior, dorsal, and ventral) as a spatial reference. The number of apoptotic cells was more than two times higher in the anterior-dorsal compartment than in the others (Figures 1J–1L pairwise t test  $p \leq 0.056$ ). This suggested that the spatial bias emerges at least during early L3 stage and persists for more than 24 h. We then checked whether this pattern was indeed dependent on core regulators of apoptosis/caspases. Co-expression of GC3Ai with a dominant negative allele of Dronc (*Drosophila* caspase-9) significantly reduced the amount of GC3Ai signal and reduced the spatial bias (Figures 1H, S1L–S1N, and S1S). Similarly, depletion of the pro-apoptotic gene *hid* by RNAi in the wing pouch almost completely abolished the GC3Ai signal (Figures 1I, S1O–S1Q, and S1S). Finally, the number of TUNEL-positive cells was significantly reduced in a *dark*<sup>(CD4)</sup> mutant background (*Drosophila* Apaf1/apoptosome protein<sup>46</sup>), specifically in the apoptosis hot-spots regions (Figures S1R, S1R', and S1T, compared with Figure S1K). These observations suggest that the spatial bias is at least in part caspase-dependent and most likely relies on the expression of the pro-apoptotic gene *hid* and on the

apoptosome. Accordingly, we found a slight but systematic and reproducible increase of *hid* expression near the GC3Ai hot spot region, using a GFP insertion at the *hid* locus<sup>47</sup> (Figures 1M and 1N). Note, however, that other factors may also contribute to the spatial bias, as we still observed some heterogeneity in cell death distribution upon Dronc inhibition or *hid* depletion (Figures S1N, S1Q, and S1S).<sup>12</sup> We also checked the pattern of expression of other pro- and anti-apoptotic genes, namely *reaper*, *grim*, and *diap1* (Figures S2A–S2C'). Although none of them specifically matched the full pattern of apoptosis, we did find some partial overlap between local increase of apoptosis in the proximal intervein L3-L4 regions of the disc and *reaper* expression (Figures S2A and S2A'). This suggested that the pattern of apoptosis strongly relies on *hid* but may be influenced by the pattern of expression of other core regulators of apoptosis.

Altogether, we conclude that contrary to what was previously observed<sup>12,23</sup> apoptosis is not spatially homogeneous in the wing imaginal disc and that some regions (anterior and close to the DV boundary, dorsal compartment) undergo higher rates of apoptosis. These hotspots are in part explained by a spatial bias in the expression of the pro-apoptotic gene *hid* but are also likely to be regulated by other factors.

### The spatial bias in apoptosis influences clonal disappearance and local net growth

We next checked whether this spatial bias in apoptosis could have any consequence on clonal dynamics and local growth. Since ex vivo live imaging of the wing disc does not allow long-term tracking of cell fate and local growth, we used an alternative approach based on twin clone labeling. We used the mosaic analysis with a repressible cell marker (QMRCM) technique<sup>48</sup> to stain the two daughter cells generated after mitotic recombination and their progeny with different fluorescent markers using alternate sets of transcription factors (Gal4 or the Qsystem, Figures 2A and 2B). Since cell movements and cell-cell intercalations are relatively neglectable in the wing disc,<sup>49,50</sup> the spatial proximity of patches of cells marked with GFP and RFP can be unambiguously attributed to a twin clone in conditions of low frequency of clone induction. We assessed the probability of clone disappearance by scoring the number of single-colored clones that are not in the vicinity of the other sibling clone 48 h after clone induction. Such an observation can only be explained by the early disappearance of the lineage of the other daughter cell and thus identifies a clone disappearance event (Figure 2A). We first noted that the QMRCM system has an intrinsic bias toward smaller clones and higher probability of clone disappearance for GFP/Gal4 clones relative to RFP/QF ones (Figure S2D), most likely due to the inherent toxicity of Gal4.<sup>51</sup> Although in this context we cannot extrapolate on the absolute probability of clone disappearance, this should not preclude the analysis of potential spatial biases. By multiplexing a large number of discs and using the same spatial landmarks as those used in

clone occurrences with twin spot QMRCM system, in control conditions (C) and by expressing UAS-Dronc<sup>DN</sup> in the GFP clone (C'). (C) and (C') share the same color scale. (D) Right: spatial map of single clone occurrences for twin clones using mitotic recombination and the H99 deletion (covering the pro-apoptotic genes *hid*, *grim*, and *reaper*) with *arm-LacZ* allele to mark the sister WT chromosome, left scheme shows the β-gal signal associated with each genotype (dark: homozygous mutant, 2 β-gal copies: WT, 1 copy: heterozygous). A representative wing disc is shown on the bottom left (green: β-gal). White stars show twin clones, dotted square, and close-up view of an example of single H99 mutant clone. Scale bars, 50 μm. See also Figure S2.

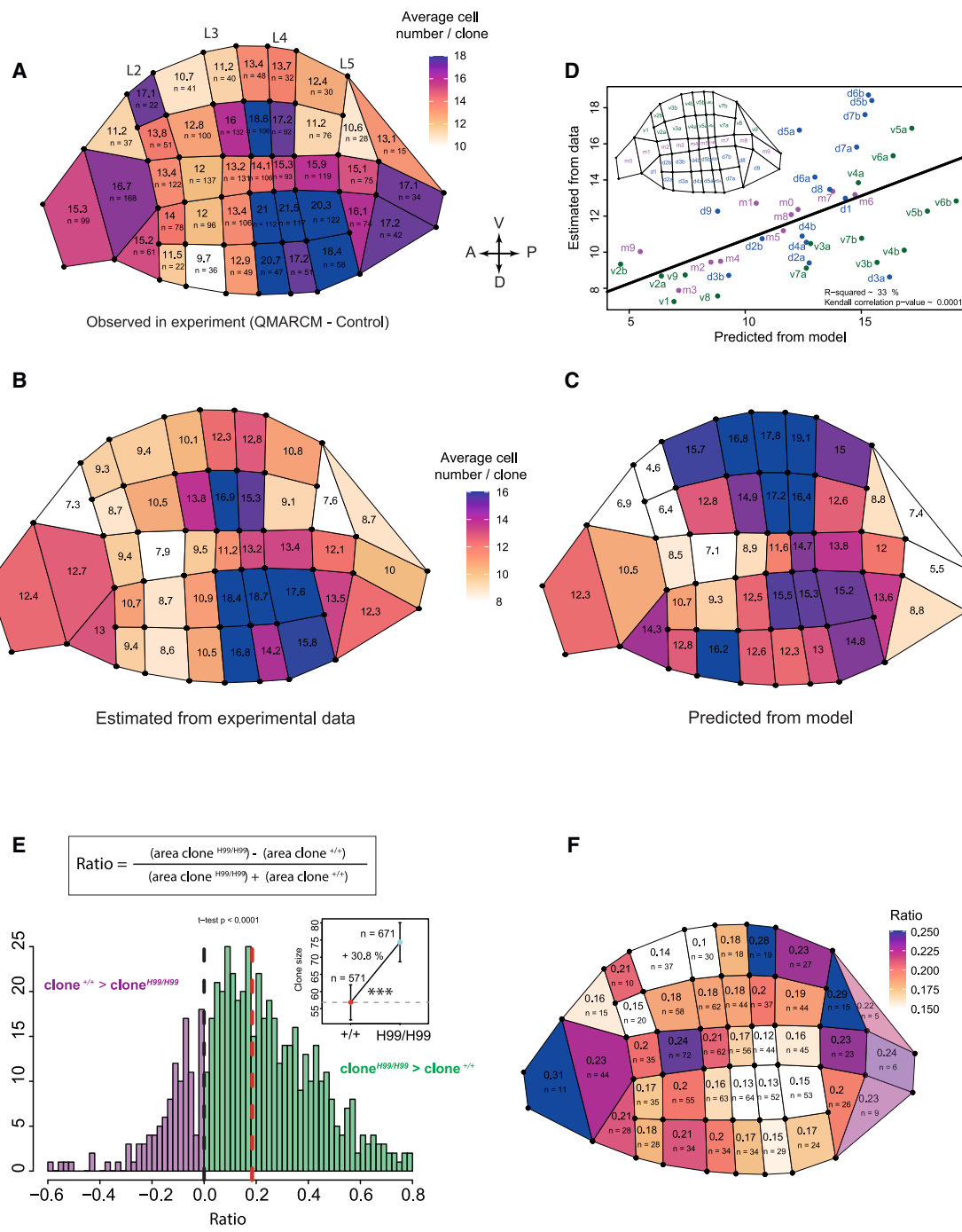


**Figure 3.** Spatial variation of apoptosis modulates local growth and clone size

(A) Spatial map for average cell number per clone in QMRCM – control experiment. Clones were considered irrespective of their color. For each compartment, the average clone surface was calculated and divided a posteriori by the average cell apical size obtained in the same compartment to obtain an estimation of the averaged cell number per clone (see STAR Methods and Figure S3).

(B) Spatial map of the mean value of clone size ( $\mu(t)$ , see STAR Methods), which integrates the experimental average clone size as well as the 0 values (estimated from the proportion of single color clone, see STAR Methods).

(C) Spatial map of the averaged predicted number of cells per clone assuming a constant and homogeneous growth rate throughout the pouch and heterogeneous rate of apoptosis, estimated from the local proportion of single colored clone (see STAR Methods). (B) and (C) share the same color scale bar.

(D) Correlation between the average cell number per clone predicted from the model and estimated from experimental data for each compartment. The black line is the linear regression. The R-squared of the regression and the p value of a correlation test (Kendall) are shown. One dot = one compartment, colored and named according to the map shown on the left side of the plot (blue: dorsal compartments d1 to d9; magenta: margin compartments m0 to m9; green: ventral compartments v1 to v9).

**Figure S1C** (Figure 2B), we obtained a coarse-grained spatial map of the probability of clone disappearance (Figure 2C). Strikingly, we observed that similar to caspase activation in the tissue, the probability of clone disappearance is not spatially homogeneous (Moran's test  $p < 0.001$ ). We identified clear hotspots of clone death, including the anterior-dorsal region near the DV boundary (~2-fold increase, compared with posterior compartments at similar DV positions, Figures 2C and S2E), as already outlined by the caspase-positive cells' mapping (Figure 1G). Note that this clone strategy reflects the pattern of apoptosis at earlier stages of development (most likely around the time of clone induction, early L2), compared with the one revealed with apoptotic markers. Nevertheless, we still observed a significant compartment-to-compartment correlation between GC3Ai levels and clone disappearance probability (weighted Pearson's correlation = 0.38,  $p = 0.016$ ). Importantly, clone size was also on average smaller (estimated through total apical surface and number of cells) in regions showing high rates of apoptosis and clone disappearance (Figures 3A and S3C). This suggested that spatial biases in caspase activity not only modulate the probability of clone survival but also the cumulative local growth in the wing disc. Indeed, these local differences in clone size match the differences numerically estimated from an exponential growth model with no spatial difference in proliferation rate, including the spatial differences in apoptotic rates calculated from our measurements of clone disappearance (see STAR Methods; Figures 3B–3D). This indicates that local differences in clone size could be solely explained by spatial differences in apoptotic rates. To check whether these spatial differences are indeed driven by caspases, we repeated the QMARCM clonal assay upon inhibition of caspase in the Gal4 sibling clones (using UAS-Dronc<sup>DN</sup>). Although this did not totally abolish clone disappearance, the spatial pattern was flattened with no visible hot spot of clone disappearance in the anterior side (Figures 2C' and S2E, Moran's test  $p = 0.11$ , no significant spatial bias; Pearson's correlation with wild-type (WT) QMARCM single clone pattern = 0.078,  $p = 0.63$ ) and led to a more homogeneous clone size between anterior and posterior compartment (Figure S3D). To confirm the effect of caspases and to check whether a similar pattern could be observed in the absence of Gal4, we also used mitotic clones in the H99/+ background (a deletion covering the three pro-apoptotic genes *hid*, *grim*, and *reaper*<sup>52</sup>), generating on the one hand H99 homozygous mutant clones (resistant for apoptosis) as well as a WT sibling. Although we observed globally less single clones, compared with the QMARCM approach (confirming the impact of Gal4 on clone disappearance probability), single H99 clones (loss of WT sibling) were markedly more frequent near the hot-spots of apoptosis (Figure 2D, Moran's test for spatial heterogeneity,  $p = 0.003$ , Pearson's correlation with GC3Ai pattern: 0.41,  $p = 0.009$ ) and completely biased toward WT clone disappearance. This confirmed the pattern of clone disappearance

observed with QMARCM in the absence of any possible bias caused by Gal4 toxicity. H99 mutant clones were almost systematically larger than their WT siblings (Figure 3E, 30.8% larger on average,  $t$  test  $p < 0.0001$ ), and this bias was notably high in the hot spot of apoptosis in the margin region at the intervein L2-L3 region (ratio = 0.24,  $n = 72$ ) (Figures 3F, S3E, and S3F). Induction of neutral mitotic clones (marked with 2 copies of EGFPnls versus 2 copies of  $\beta$ -gal) on the contrary shows an almost perfectly symmetric distribution of clone size between the two siblings, with no asymmetry of probability of clone disappearance, and yet a similar global probability of clone disappearance, compared with WT clones in H99/+ background (7% versus 8.2%, Figures S2F, S2G, S3G, and S3H). Moreover, we could also recapitulate a similar spatial bias of clone disappearance and clone size (Figures S2G and S3G). Altogether, this confirmed that (1) the spatial bias of clone disappearance can also be observed in the absence of Gal4, (2) clone disappearance is apoptosis dependent, and (3) apoptosis has a net-negative impact on local growth, especially in the apoptotic hotspots regions (Figure 1).

We conclude that the spatial bias in apoptosis generates hot-spots of clone disappearance, which also significantly reduce local growth rate mostly in the anterior-dorsal region near the DV boundary. This suggests that local increases of apoptosis could play an instructive role by reducing local growth, which therefore may affect the final shape and size of the tissue.

#### Patterned apoptosis in the larvae and in the pupae modulates adult wing shape and size

We therefore checked whether local biases in apoptosis could significantly impact adult wing shape and size. To obtain a precise and quantitative description of adult wing shape and size, we used a quantitative assay based on semi-automatic wing segmentation, landmark positioning, and Procrustes alignment of wings (which includes translation, rotation, and global rescaling)<sup>53,54</sup> (Figure S4A). To analyze the impact of apoptosis in the wing proper, we used the Nab-Gal4 driver, one of the few drivers well restricted to the pouch both at larval and pupal stage (Figure 4A). Interestingly, inhibition of cell death in the wing tissue, using *hid* RNAi or a microRNA targeting *hid*, *grim*, and *reaper* (mirRHG<sup>55</sup>), led to a significant increase in wing size (Figures 4B and 4C, 8.7% and 4.2%, respectively, a similar range to what was obtained upon ectopic overexpression of Dp110/phosphatidylinositol 3-kinase [PI3K]<sup>56</sup>), suggesting that apoptosis has a net-negative effect on adult tissue size. *Hid*-double-stranded RNA (dsRNA) and mirRHG effect on *hid* mRNA levels were confirmed by RT-PCR (see STAR Methods). We also observed significant changes in adult wing shape, including a relative increase in the size of the most anterior and posterior domains, as well as a global wing rounding (Figure 4D). To check whether local increases in apoptosis were indeed responsible for the local modulation of shape and size, we

(E) Distribution of twin-clone area ratio values for each H99 mitotic clone (H99 homozygous mutant versus WT sibling clone, see top formula). Negative ratios: WT clone bigger than H99 clone, positive ratios: H99 clone bigger than WT clone. Black dotted line shows 0 (= equal clone size), red dotted line the median of the distribution. Top right inset shows the bulk averaged clone size (30.8% bigger for H99 compared with WT,  $p < 0.0001$ ), dots averages, error bars 95% confidence intervals,  $n$ , number of clones. Single clones were not used for these comparisons (which would have a value of +1 or -1). \*\*\*  $p < 0.0001$  ( $t$  test).

(F) Spatial map for averaged clone size ratio for H99 and WT sibling clones (see in E) for each of the 40 compartments of 66 wing discs. Color scale is shown on the right. See also Figure S3.

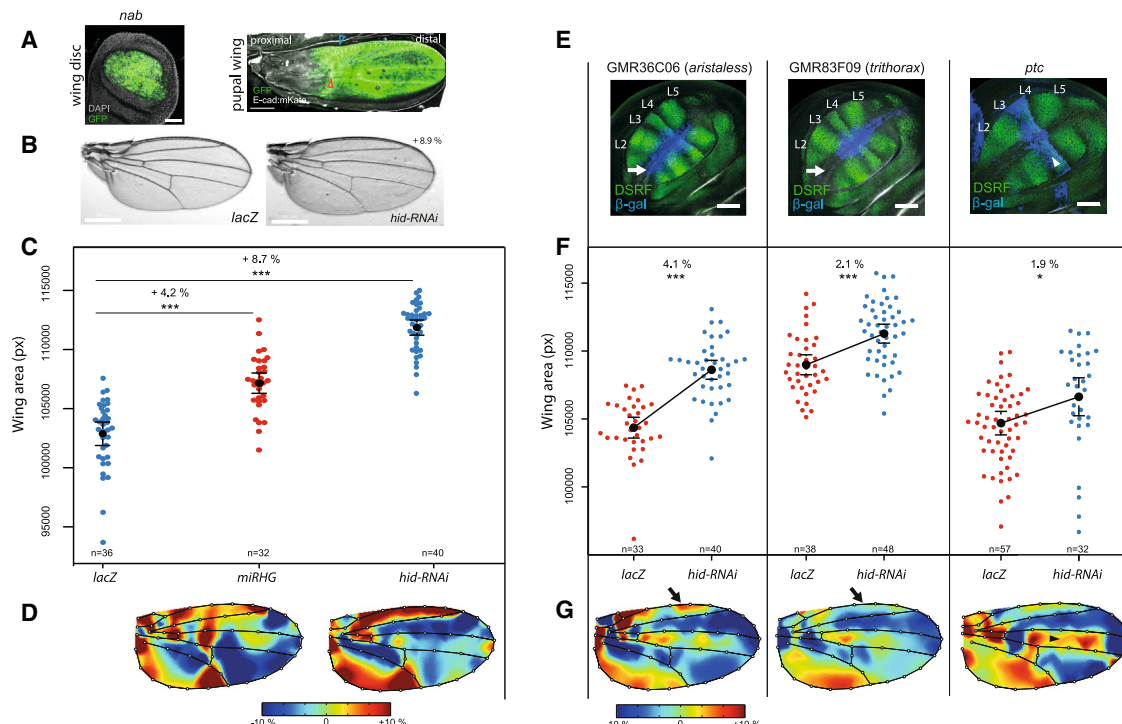


**Figure 4. Apoptosis locally and globally affects wing size and shape**

(A) Pattern of expression at ~96 h AEL of the Nab-GAL4 driver used to express *hid-RNAi* at larval stage (left, GFP, green) and pupal stage (right, 30 h APF, GFP, green, E-cad::mKate,<sup>57</sup> magenta, red and blue arrowhead point at the hinge/blade boundary recognized by the accumulation of E-cad along antero-posterior axis (red arrowhead) and the infold on the anterior side (blue arrowhead). Scale bars, 50 µm top and 200 µm bottom.

(B) Representative images of adult wings in the control (*Nab-GAL4, UAS-LacZ*) and upon downregulation of apoptosis by *hid* depletion (*Nab-GAL4, hid-RNAi*). Wings are bigger and slightly rounder. Scale bars, 500 µm.

(C) Variation of adult wing size in control (*UAS-LacZ*), upon expression of the microRNA targeting *hid*, *grim*, and *reaper* (*miRHG*) and depletion of Hid (*hid-RNAi*) all with the Nab-GAL4 driver. Each dot is a wing. Black dots are means and error bars 95% confidence interval. n, number of wings. \*\*\*p < 0.0001 (t test).

(D) Local variation of tissue shape caused by expressing *miRHG* or *hid-RNAi* relative to the control wing (*lacZ*). Colors represent changes in relative area necessary to transform the average wing from the control group to the perturbed group after alignment, rotation, and size normalization, red expansion, blue shrinkage (number of wings shown in C). Note that this comparison is done after rescaling the wings in order to compare variations of shape. Color bar shows the upper and lower limits in deformation. Left: proximal, right: distal, top: anterior, bottom: posterior.

(E) Pattern of expression in the wing disc at ~96 h AEL of various GAL4 drivers used to express *hid-RNAi*. Green, DSRF, blue, UAS-β-gal. L2, L3, L4, and L5 show the different prospective veins. White arrows show the most anterior region of the disc, where GAL4 is expressed in the case of *aristaless-GAL4* but not in the case of *tritrophic-GAL4*. Scale bars, 50 µm. Left: anterior, right: posterior, top: ventral, bottom: dorsal.

(F) Variation of adult wing size for the different genotypes. Each dot is a wing. Black dots are means and error bars 95% confidence interval. n, number of wings. \*\*\*p < 0.0001, \*p = 0.02 (t test).

(G) Local variations of tissue shape caused by expressing *hid-RNAi* relative to the control wing (*lacZ*) for each GAL4 driver. Colors represent changes in relative area necessary to transform the average wing from the control group to the perturbed group, red expansion, blue shrinkage (number of wings shown in F). Left: proximal, right: distal, top: anterior, bottom: posterior. See also Figure S4.

used various drivers to inhibit apoptosis in different wing subdomains (Figure 4E). Accordingly, inhibition of *hid* in the patched domain (*ptc-gal4*, expressed in a band at the intervein L3-L4, Figure 4E, white arrowhead) led to a global increase of wing size characterized by the expansion of the region overlapping the *ptc* domain (Figures 4F and 4G, black arrowhead). This suggested that apoptosis has a local impact on growth even in regions other than the apoptosis hotspots identified at larval stage. We also used drivers restricted to the DV boundary either in the anterior (*aristaless-GAL4*, encompassing the caspase hot spot) or posterior part of the wing disc (*tritrophic-GAL4*) (Figure 4E, white arrows). Interestingly, while *hid* depletion in the posterior-DV boundary domain had a mild effect on wing size (Figures 4F and 4G, 2.1%), similar to inhibition of *hid* in the ptc

domain), this effect was enhanced upon inhibition in the anterior-DV boundary domain (4.1%, Figures 4F and 4G, black arrows). Importantly, the expansion of the most anterior domain of the wing was only observed upon inhibition of *hid* in the anterior-DV boundary domain (Figures 4F and 4G). Altogether, this suggests that apoptosis has a local negative effect on wing domain size, which is more significant in regions overlapping hotspots of apoptosis characterized in the wing imaginal disc.

So far, our perturbative approaches did not allow to distinguish the contributions of apoptosis during larval or pupal stage, where significant tissue size and shape modulation can still take place.<sup>27,36,37,58</sup> Therefore, we also performed experiments with conditional *hid* depletion under the control of a temperature-sensitive driver (Gal4 combined with Gal80<sup>ts</sup>) to assess the relative

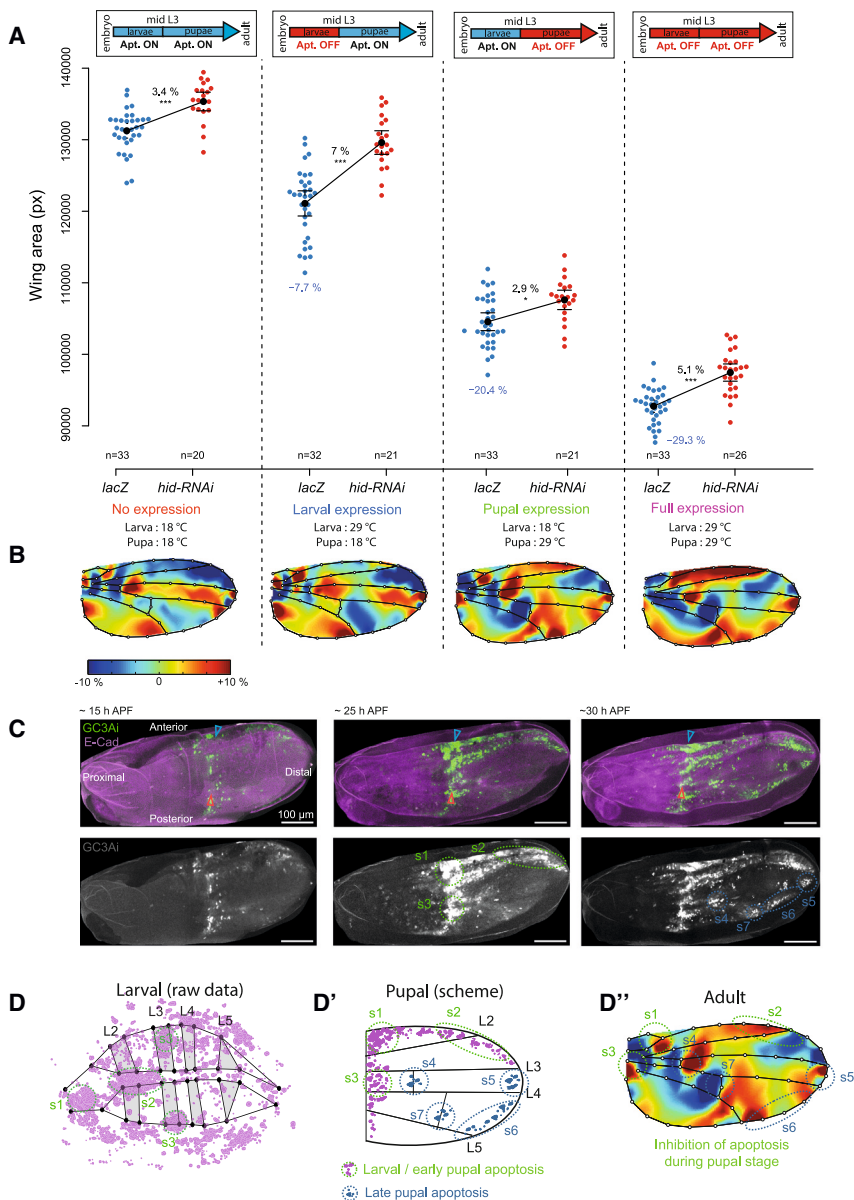


**Figure 5. Larval and pupal patterned apoptosis affects adult wing size and shape**

(A) Variation of adult wing size in control (*UAS-LacZ*) and upon depletion of Hid (*hid-RNAi*) with the Nab-GAL4 driver and conditional activation at different developmental stages, using the thermosensitive GAL4 inhibitor *GAL80<sup>TS</sup>* and controlled temperature shift (29°C, Hid depletion, 18°C no Hid inhibition). See Figure S4. The % in black shows the variation between the Hid RNAi and corresponding control. The % in blue shows the variation of size for the control at a given temperature relative to the 18°C control (no expression). The top schemes show the period of development during which apoptosis is inhibited. One dot = one wing. Black dots: means, error bars: 95% confidence interval. n, number of wings. \*\*\*p < 0.0001, \*p = 0.001 (t test).

(B) Local variation of tissue shape caused by expressing *hid-RNAi* relative to the control wing (*lacZ*) for each temperature condition. Colors represent changes in relative area necessary to transform the average wing from the control group to the perturbed group, red expansion, blue shrinkage (number of wings shown in A). Left: proximal, right: distal, top: anterior, bottom: posterior.

(C) z-local projections of a live pupal wing expressing *UAS-GC3Ai* (green) in the Nab-GAL4 domain (wing pouch) and E-cad::mKate (magenta) between 16 and 32 h APF (hours after pupal formation). See Video S1. Representative of 4 movies. s1 to s3 and green ellipses show early domains of apoptosis (already appearing at 16 h APF), and s4 to s7 and blue ellipses show late domains of apoptosis (appearing around 30 h APF). Blue and red arrowheads show the position of the margin between the blade and hinge. Scale bars, 100 μm.

(D) Averaged pattern of apoptosis in the wing disc (Figure 1F) and the corresponding early pupal apoptosis zones (s1 to s3, green ellipses). Anterior: left, posterior: right, ventral: top, dorsal: bottom.

(D') Schematic of the apoptosis pattern observed in the pupal wing with early domains (s1 to s3, green ellipses) and late domains (s4 to s7, blue ellipses). Note the correspondence between early domains and the pattern of apoptosis observed in the wing disc (D, magenta dots). Left: proximal, right: distal, top: anterior, bottom: posterior.

(D'') Map of wing deformation associated with Hid inhibition at pupal stage (B, pupal expression) and the position of the pupal apoptosis zones. Left: proximal, right: distal, top: anterior, bottom: posterior. See also Figures S4 and S5 and Video S1.

contribution of *hid* expression at larval stage versus pupal stage to the final wing shape and size (Figures S4B and S4C). Despite the strong confounding effect of temperature on wing size,<sup>59</sup> we found that *hid* depletion at larval stage (up to mid L3) had a significant impact on adult wing size (Figure 5A, larval expression, +7%, t test p < 0.001), whereas depletion during pupal stage had a milder effect (Figure 5A, pupal expression, +2.9%, similar to the background effect observed in the negative control, +3.4%, the absence of significant effect was confirmed by bootstrapping). This suggested that larval apoptosis had a significant negative contribution to global wing size. We then analyzed the relative contribution of larval and pupal apoptosis to final adult wing shape. Surprisingly, this

revealed that the wing shape modulation observed upon persistent *hid* downregulation could be partially recapitulated by pupal inhibition of *hid* (compare Figure 5B, pupal expression and full expression, with Figure 4D), suggesting that pupal apoptosis also contributes to adult wing shape. We next used principal-component analysis (PCA) to decompose the main contributors of shape variation and compare unambiguously and quantitatively wing shape between conditions. Removing the effect of temperature (principal component 1) outlined the contribution of shape variation (principal component 3 [PC3]), which is going along the same direction for larval, pupal, and full depletion of Hid (Figures S5A and S5B). Interestingly, the amplitude of variation along PC3 for Hid full depletion matches the sum of

variations observed for larval and pupal depletion, suggesting that adult wing shape is generated by the cumulative effect of larval and pupal inhibition of apoptosis, which has similar effects on shape. Variations along PC3 mostly recapitulate global wing rounding (Figure S5C wing deformation between the two extreme values along PC3) in good agreement with the shape modulation observed for Hid depletion throughout development (Figures 4B and 4D).

This prompted us to evaluate the pattern of apoptosis in the pupal wing. We performed live imaging of pupal wings between 16 and 35 h APF, expressing GC3Ai in the pouch (using the Nab-Gal4 driver). This revealed striking dynamics of apoptosis with an early concentration in the most anterior part of the wing as well as the junction with the hinge (Figure 5C; Video S1). This pattern shows an interesting correspondence with the hotspots observed at larval stage (Figures 5C–5D'), suggesting that the spatial biases present at larval stage are for a good part maintained during pupal development. Nevertheless, the pattern of apoptosis is dynamic as new hotspots of apoptosis appear at later (~30 h APF) pupal stage (Figures 5C and 5D'). Importantly, the domains of high GC3Ai expression and apoptosis match the regions more significantly deformed in the adult wing upon pupal inhibition of Hid (compare Figure 5C, Video S1, and Figure 5D'). Using ubiquitous expression of GC3Ai driven by lexA, we also confirmed that restricted larval expression of hid-dsRNA using Nab-Gal4 and Gal80ts does not impact caspase activity in the pupal wing blade, while pupal expression of hid-dsRNA reduced GC3Ai signal in the pupal wing blade (Figures S5D and S5E).

Altogether, we conclude that spatial biases in apoptosis distribution in the growing wing can significantly modify the size and shape of the adult wing, by modulating morphogenesis either during early larval stages or during later pupal ones. This suggests that the fine spatial tuning of apoptosis in a fast-growing tissue plays an instructive role for organ shape and size regulation.

## DISCUSSION

In this study, we outlined an unexpected pattern of apoptosis in the growing wing imaginal disc with a significant upregulation in the anterior and dorsal compartment of the wing. Part of this pattern is preserved during pupal stage and contributes to pupal wing morphogenesis. Moreover, our quantitative assessments of clonal growth and adult wing shape clearly show that this local upregulation of apoptosis has a significant impact on local net growth and final adult shape and size. Most likely, local upregulation of apoptosis fine-tune wing shape by locally reducing the number of cells and altering the relative proportion of wing sub-domains, although at this stage nothing excludes a more complicated contribution through an apoptosis-dependent modulation of tissue mechanics and/or signaling pathways. So far, the characterization of cell death has never been performed in a systematic manner using spatial landmarks that allow for superimposition of data from many individuals, which may explain why such biases have been missed.<sup>23</sup> Similarly, the impact of apoptosis on tissue shape and size has never been studied with such quantitative readouts. Our work emphasizes the need for more systematic quantitative assessments of death distribution in order to evaluate its contribution to organ shape/size regulation. The

pipeline used in this study may easily be applied in other developmental contexts that are not amenable for long-term live imaging, as long as markers can be used for spatial registration and tools are available for clone generation.

Previous work suggested that sublethal caspase activation also contributes to wing disc growth regulation and adult tissue size; however, in this situation, basal caspase activity promotes growth and effector caspase inhibition through p35 overexpression rather reduces wing size.<sup>44</sup> However, this effect is not visible upon inhibition of upstream regulators of caspases, which was interpreted by the absence of inhibition of the pro-growth basal effector caspase activity. In this study, we purposefully used upstream inhibitors of apoptosis to avoid this effect, which now revealed an increase of local growth and wing size upon apoptosis inhibition. Our live imaging data on the pupal wing also suggests the existence of a significant proportion of cell death in the hinge region (Video S1; Figures 5C–5D'). Interestingly, our preliminary observations using hinge-specific driver suggest that apoptosis inhibition in the hinge rather reduces adult wing size (not shown). This is in sharp contrast with the effect we observed upon inhibition in the pouch and suggests that the interpretation of wing shape phenotype requires to precisely monitor the domains of perturbations, especially for commonly used Gal4 encompassing both pouch and hinge region (e.g., nubbin-Gal4). Although we focused here on tissue autonomous contribution of cell death, future work will help to decipher the putative contribution of hinge apoptosis to final wing size and shape through a non-tissue autonomous effect.

Compensatory proliferation is one of the best-studied processes that relates apoptosis to the induction of cell proliferation.<sup>60</sup> So far, this process was mostly characterized either in conditions of massive death induction through irradiation and genetic induction of apoptosis in large domains<sup>61,62</sup> or through the perturbation of the core apoptotic pathway (e.g., by blocking some of the essential caspases, caspase-3 in *Drosophila*<sup>63</sup> or caspase-9 in mammalian epidermis<sup>64</sup>). However, to our knowledge, there is no study that has clearly identified biases in cell proliferation distribution in the vicinity of physiological apoptosis *in vivo*. Surprisingly, we observed a net-negative effect of the local increase of cell death on local clone size and the size of the final adult compartment, and we also outlined a significant effect of physiological death on the final size of the adult wing (Figures 2, 4, and 5). This suggests that compensatory proliferation is unlikely to occur in the context of physiological apoptosis, or at least that its contribution is relatively minor and not sufficient to compensate for cell loss by apoptosis. Further quantitative studies of the coupling between apoptosis and cell proliferation will be essential to assess its real contribution to physiological growth regulation. Interestingly, a recent study outlined a significant positive upregulation of proliferation near dying MDCK Madin-Darby canine kidney cells; however, this effect is strongly context dependent and is not visible at low stiffness or high density values,<sup>65</sup> conditions that may apply to the wing imaginal disc.

Cell competition is the process describing the context-dependent elimination of viable but suboptimal cells.<sup>6</sup> Studies of clonal elimination in the wing imaginal disc have thoroughly contributed to our understanding of this process. Interestingly, most of these studies assumed that clone disappearance in

physiological conditions is largely neglectable. Our results suggest that WT clones can undergo early elimination in the wing imaginal disc and that this elimination is spatially biased, although we should remain cautious when extrapolating the absolute probability of clone elimination, compared with the experimental conditions used in this study. On the one hand, this opens the possibility for spontaneous competition occurring in the wing imaginal disc, which so far has not been thoroughly explored (although its existence has been suggested by indirect genetic evidence<sup>12,41,66</sup>). On the other hand, it also suggests that cell elimination during competition may be influenced by this spatial pattern of caspase activity and apoptosis. Further quantitative description of clonal elimination during competition may reveal such spatial bias and would help to study the influence of pre-existing patterns of caspases/apoptosis on cell competition and tissue plasticity.

In this study, we showed that local modulation of *hid* expression can fine-tune the local level of apoptosis, which will impact local growth and adult tissue shape in a subtle and quantitative way, similarly to the phenotypic changes observed at the macro-evolutionary scale.<sup>67</sup> Thus, the evolution of the *cis*-regulatory elements of pro-apoptotic genes may constitute an additional lever for shape evolution that could be used to fine-tune adult appendage shape. It would be important in this perspective to understand which factors fine-tune the expression levels and the pattern of pro-apoptotic genes and to dissect how they might be modulated during evolution. Interestingly, these pro-apoptotic genes are most likely less pleiotropic than pro-proliferative pathways such as morphogens, receptor tyrosine kinase (RTK) signaling pathways, or Hippo pathways that are classically studied for the regulation of size and growth.<sup>15</sup> Therefore, modulating pro-apoptotic genes levels and pattern of expression may constitute a relatively parsimonious way to evolve wing and appendage shape.

## STAR★METHODS

Detailed methods are provided in the online version of this paper and include the following:

- KEY RESOURCES TABLE
- RESOURCE AVAILABILITY
  - Lead contact
  - Materials availability
  - Data and code availability
- EXPERIMENTAL MODEL AND SUBJECT DETAILS
  - Drosophila melanogaster husbandry
  - Drosophila melanogaster strains
- METHOD DETAILS
  - Design of lexAOP-GC3Ai fly line
  - QPCR validation of Hid depletion
  - Immunostaining
  - Live imaging of pupal wing
- QUANTIFICATION AND STATISTICAL ANALYSIS
  - Image processing
  - QMARM and mitotic clones experiments
  - Spatial maps of wing discs (twin clones and GC3Ai)
  - Adult wing shape and size analyses

- Estimation of clone size differences in an exponential growth regime
- Estimation of the clone extinction probability
- Estimation of the clone size and relationship with apoptosis and proliferation rate
- Estimating the apoptosis and proliferation rates for each compartment
- Estimating the expected differences of clone size between compartments assuming constant proliferation rate
- Statistical analysis

## SUPPLEMENTAL INFORMATION

Supplemental information can be found online at <https://doi.org/10.1016/j.cub.2023.12.031>.

## ACKNOWLEDGMENTS

We thank members of the R.L. lab for critical reading of the manuscript. We would like to thank Christina Fissoun, Lucia Rodriguez Vazquez, Gaurav Shajpal, and Delia Cicciarello for their contribution to adult wing and wing disc analysis during their internship. We are also grateful to Jean-Paul Vincent, Magali Suzanne, David Houle, Seth Blair, Andrea Bergman, Yohanns Bel-laiche, Jae Park, the Bloomington Drosophila Stock Center, the Drosophila Genetic Resource Center, and the Vienna Drosophila Resource Center, Flybase for sharing essential information, stocks, and reagents. We also thank Benoit Aigouy for the Packing Analyser software, Raphaël Etournay for very helpful guidance on pupal wing live imaging, and Jean-Yves Timévez and the image analysis platform of Institut Pasteur for the LocalZprojector plugin on Fiji. Work in R.L. lab is supported by the Institut Pasteur (G5 starting package), the ERC starting grant CoSpaDD (Competition for Space in Development and Disease, grant no. 758457), the ANR-10-LABX-0073, the Cercle FSER, and the CNRS (UMR 3738).

## AUTHOR CONTRIBUTIONS

R.L. and A.M.-V. discussed and designed the project and wrote the manuscript. T.C. performed part of the experiments on adult wing shape and twin clones analysis, as well as the wing disc segmentation. F.L. participated in adult wing dissection, imaging, and segmentation; performed the RT-PCR; and generated the lexAOP-GC3Ai line. A.D. provided the theoretical calculation of the expected distribution of clone size based on differences in apoptotic rates. A.M.-V. performed all the other experiments and analyses. Every author has commented on and edited the manuscript.

## DECLARATION OF INTERESTS

The authors declare no competing interests.

Received: April 21, 2022

Revised: July 13, 2023

Accepted: December 11, 2023

Published: January 11, 2024

## REFERENCES

1. Lecuit, T., and Le Goff, L. (2007). Orchestrating size and shape during morphogenesis. *Nature* **450**, 189–192.
2. Fuchs, Y., and Steller, H. (2011). Programmed cell death in animal development and disease. *Cell* **147**, 742–758.
3. Toyama, Y., Peralta, X.G., Wells, A.R., Kiehart, D.P., and Edwards, G.S. (2008). Apoptotic force and tissue dynamics during Drosophila embryogenesis. *Science* **321**, 1683–1686.

4. Monier, B., Gettings, M., Gay, G., Mangeat, T., Schott, S., Guarner, A., and Suzanne, M. (2015). Apico-basal forces exerted by apoptotic cells drive epithelium folding. *Nature* **518**, 245–248.
5. Roellig, D., Theis, S., Proag, A., Allio, G., Bénazéraf, B., Gros, J., and Suzanne, M. (2022). Force-generating apoptotic cells orchestrate avian neural tube bending. *Dev. Cell* **57**, 707–718.e6.
6. Clavería, C., and Torres, M. (2016). Cell competition: mechanisms and physiological roles. *Annu. Rev. Cell Dev. Biol.* **32**, 411–439.
7. Adachi-Yamada, T., Fujimura-Kamada, K., Nishida, Y., and Matsumoto, K. (1999). Distortion of proximodistal information causes JNK-dependent apoptosis in *Drosophila* wing. *Nature* **400**, 166–169.
8. Adachi-Yamada, T., and O'Connor, M.B. (2002). Morphogenetic apoptosis: a mechanism for correcting discontinuities in morphogen gradients. *Dev. Biol.* **251**, 74–90.
9. Gibson, M.C., and Perrimon, N. (2005). Extrusion and death of DPP/BMP-compromised epithelial cells in the developing *Drosophila* wing. *Science* **307**, 1785–1789.
10. Shen, J., and Dahmann, C. (2005). Extrusion of cells with inappropriate Dpp signaling from *Drosophila* wing disc epithelia. *Science* **307**, 1789–1790.
11. Bielmeier, C., Alt, S., Weichselberger, V., La Fortezza, M., Harz, H., Jülicher, F., Salbreux, G., and Classen, A.K. (2016). Interface contractility between differently fated cells drives cell elimination and cyst formation. *Curr. Biol.* **26**, 563–574.
12. Merino, M.M., Seum, C., Dubois, M., and Gonzalez-Gaitan, M. (2022). A role for flower and cell death in controlling morphogen gradient scaling. *Nat. Cell Biol.* **24**, 424–433.
13. Boulan, L., and Léopold, P. (2021). What determines organ size during development and regeneration? *Development* **148**, dev196063.
14. Vollmer, J., Casares, F., and Iber, D. (2017). Growth and size control during development. *Open Biol.* **7**, 170190.
15. Hariharan, I.K. (2015). Organ size control: lessons from *Drosophila*. *Dev. Cell* **34**, 255–265.
16. Wartlick, O., Mumcu, P., Kicheva, A., Bittig, T., Seum, C., Jülicher, F., and González-Gaitán, M. (2011). Dynamics of Dpp signaling and proliferation control. *Science* **331**, 1154–1159.
17. Harmansa, S., Hamaratoglu, F., Affolter, M., and Caussinus, E. (2015). Dpp spreading is required for medial but not for lateral wing disc growth. *Nature* **527**, 317–322.
18. Strassburger, K., Lutz, M., Müller, S., and Teleman, A.A. (2021). Ecdysone regulates *Drosophila* wing disc size via a TORC1 dependent mechanism. *Nat. Commun.* **12**, 6684.
19. Akiyama, T., and Gibson, M.C. (2015). Decapentaplegic and growth control in the developing *Drosophila* wing. *Nature* **527**, 375–378.
20. Gerhold, A.R., Richter, D.J., Yu, A.S., and Hariharan, I.K. (2011). Identification and characterization of genes required for compensatory growth in *Drosophila*. *Genetics* **189**, 1309–1326.
21. Hecht, S., Perez-Mockus, G., Schienstock, D., Recasens-Alvarez, C., Merino-Aceituno, S., Smith, M., Salbreux, G., Degond, P., and Vincent, J.P. (2022). Mechanical constraints to cell-cycle progression in a pseudostratified epithelium. *Curr. Biol.* **32**, 2076–2083.e2.
22. Voss, A.K., and Strasser, A. (2020). The essentials of developmental apoptosis. *F1000Res* **9**. F1000 Faculty Rev-148.
23. Milán, M., Campuzano, S., and García-Bellido, A. (1997). Developmental parameters of cell death in the wing disc of *Drosophila*. *Proc. Natl. Acad. Sci. USA* **94**, 5691–5696.
24. Mailleux, A.A., Overholtzer, M., Schmelzle, T., Bouillet, P., Strasser, A., and Brugge, J.S. (2007). BIM regulates apoptosis during mammary ductal morphogenesis, and its absence reveals alternative cell death mechanisms. *Dev. Cell* **12**, 221–234.
25. Eder, D., Aegeyer, C., and Basler, K. (2017). Forces controlling organ growth and size. *Mech. Dev.* **144**, 53–61.
26. Aigouy, B., Farhadifar, R., Staple, D.B., Sagner, A., Röper, J.C., Jülicher, F., and Eaton, S. (2010). Cell flow reorients the axis of planar polarity in the wing epithelium of *Drosophila*. *Cell* **142**, 773–786.
27. Etournay, R., Popović, M., Merkel, M., Nandi, A., Blasse, C., Aigouy, B., Brandl, H., Myers, G., Salbreux, G., Jülicher, F., et al. (2015). Interplay of cell dynamics and epithelial tension during morphogenesis of the *Drosophila* pupal wing. *eLife* **4**, e07090.
28. Romanova-Michaelides, M., Hadjivasiliou, Z., Aguilar-Hidalgo, D., Basagiannis, D., Seum, C., Dubois, M., Jülicher, F., and Gonzalez-Gaitan, M. (2022). Morphogen gradient scaling by recycling of intracellular Dpp. *Nature* **602**, 287–293.
29. Matamoro-Vidal, A., Salazar-Ciudad, I., and Houle, D. (2015). Making quantitative morphological variation from basic developmental processes: where are we? The case of the *Drosophila* wing. *Dev. Dyn.* **244**, 1058–1073.
30. Tripathi, B.K., and Irvine, K.D. (2022). The wing imaginal disc. *Genetics* **220**, iyac020.
31. Martín, F.A., Herrera, S.C., and Morata, G. (2009). Cell competition, growth and size control in the *Drosophila* wing imaginal disc. *Development* **136**, 3747–3756.
32. Garcia-Bellido, A., and Merriam, J.R. (1971). Parameters of the wing imaginal disc development of *Drosophila melanogaster*. *Dev. Biol.* **24**, 61–87.
33. Diaz de la Loza, M.C., and Thompson, B.J. (2017). Forces shaping the *Drosophila* wing. *Mech. Dev.* **144**, 23–32.
34. Srivastava, A., Pastor-Pareja, J.C., Igaki, T., Pagliarini, R., and Xu, T. (2007). Basement membrane remodeling is essential for *Drosophila* disc eversion and tumor invasion. *Proc. Natl. Acad. Sci. USA* **104**, 2721–2726.
35. Sun, T., Song, Y., Teng, D., Chen, Y., Dai, J., Ma, M., Zhang, W., and Pastor-Pareja, J.C. (2021). Atypical laminin spots and pull-generated microtubule-actin projections mediate *Drosophila* wing adhesion. *Cell Rep.* **36**, 109667.
36. Ray, R.P., Matamoro-Vidal, A., Ribeiro, P.S., Tapon, N., Houle, D., Salazar-Ciudad, I., and Thompson, B.J. (2015). Patterned anchorage to the apical extracellular matrix defines tissue shape in the developing appendages of *drosophila*. *Dev. Cell* **34**, 310–322.
37. Tsuboi, A., Fujimoto, K., and Kondo, T. (2023). Spatio-temporal remodeling of extracellular matrix orients epithelial sheet folding. *Sci. Adv.* **9**, eadh2154.
38. Peabody, N.C., and White, B.H. (2013). Ecdision gates progression of the adult ecdisis sequence of *Drosophila*. *J. Exp. Biol.* **216**, 4395–4402.
39. Abouchar, L., Petkova, M.D., Steinhardt, C.R., and Gregor, T. (2014). Fly wing vein patterns have spatial reproducibility of a single cell. *J. R. Soc. Interface* **11**, 20140443.
40. Guirao, B., Rigaud, S.U., Bosveld, F., Bailles, A., López-Gay, J., Ishihara, S., Sugimura, K., Graner, F., and Bellaïche, Y. (2015). Unified quantitative characterization of epithelial tissue development. *eLife* **4**, e08519.
41. de la Cova, C., Abril, M., Bellostá, P., Gallant, P., and Johnston, L.A. (2004). *Drosophila* myc regulates organ size by inducing cell competition. *Cell* **117**, 107–116.
42. Levayer, R., and Moreno, E. (2013). Mechanisms of cell competition: themes and variations. *J. Cell Biol.* **200**, 689–698.
43. Morata, G., and Ripoll, P. (1975). Minutes: mutants of *drosophila* autonomously affecting cell division rate. *Dev. Biol.* **42**, 211–221.
44. Shinoda, N., Hanawa, N., Chihara, T., Koto, A., and Miura, M. (2019). Dronc-independent basal executioner caspase activity sustains *Drosophila* imaginal tissue growth. *Proc. Natl. Acad. Sci. USA* **116**, 20539–20544.
45. Schott, S., Ambrosini, A., Barbaste, A., Benassayag, C., Gracia, M., Proag, A., Raye, M., Monier, B., and Suzanne, M. (2017). A fluorescent toolkit for spatiotemporal tracking of apoptotic cells in living *Drosophila* tissues. *Development* **144**, 3840–3846.
46. Rodriguez, A., Oliver, H., Zou, H., Chen, P., Wang, X., and Abrams, J.M. (1999). Dark is a *Drosophila* homologue of Apaf-1/CED-4 and functions in an evolutionarily conserved death pathway. *Nat. Cell Biol.* **1**, 272–279.

47. Crossman, S.H., Streichan, S.J., and Vincent, J.P. (2018). EGFR signaling coordinates patterning with cell survival during *Drosophila* epidermal development. *PLoS Biol.* 16, e3000027.
48. Potter, C.J., Tasic, B., Russler, E.V., Liang, L., and Luo, L. (2010). The Q system: a repressible binary system for transgene expression, lineage tracing, and mosaic analysis. *Cell* 141, 536–548.
49. Legoff, L., Rouault, H., and Lecuit, T. (2013). A global pattern of mechanical stress polarizes cell divisions and cell shape in the growing *Drosophila* wing disc. *Development* 140, 4051–4059.
50. Gibson, M.C., Patel, A.B., Nagpal, R., and Perrimon, N. (2006). The emergence of geometric order in proliferating metazoan epithelia. *Nature* 442, 1038–1041.
51. Rezával, C., Werbajh, S., and Ceriani, M.F. (2007). Neuronal death in *Drosophila* triggered by GAL4 accumulation. *Eur. J. Neurosci.* 25, 683–694.
52. White, K., Grether, M.E., Abrams, J.M., Young, L., Farrell, K., and Steller, H. (1994). Genetic control of programmed cell death in *Drosophila*. *Science* 264, 677–683.
53. Houle, D., Mezey, J., Galpern, P., and Carter, A. (2003). Automated measurement of *drosophila* wings. *BMC Evol. Biol.* 3, 25.
54. Houle, D., Van der Linde, K., and Marquez, E. (2014). Wings: automated capture of *drosophila* wing shape v. 4.0. <http://bio.fsu.edu/~dhoule/wings.html>.
55. Siegrist, S.E., Haque, N.S., Chen, C.H., Hay, B.A., and Hariharan, I.K. (2010). Inactivation of both Foxo and reaper promotes long-term adult neurogenesis in *Drosophila*. *Curr. Biol.* 20, 643–648.
56. Levers, S.J., Weinkove, D., MacDougall, L.K., Hafen, E., and Waterfield, M.D. (1996). The *Drosophila* phosphoinositide 3-kinase Dp110 promotes cell growth. *EMBO J.* 15, 6584–6594.
57. Pinheiro, D., Hannezo, E., Herszberg, S., Bosveld, F., Gaugue, I., Balakireva, M., Wang, Z., Cristo, I., Rigaud, S.U., Markova, O., et al. (2017). Transmission of cytokinesis forces via E-cadherin dilution and actomyosin flows. *Nature* 545, 103–107.
58. Blanco-Obregon, D., El Marzkioui, K., Brutscher, F., Kapoor, V., Valzania, L., Andersen, D.S., Colombani, J., Narasimha, S., McCusker, D., Léopold, P., et al. (2022). A Dilp8-dependent time window ensures tissue size adjustment in *Drosophila*. *Nat. Commun.* 13, 5629.
59. McDonald, J.M.C., Ghosh, S.M., Gascoigne, S.J.L., and Shingleton, A.W. (2018). Plasticity through canalization: the contrasting effect of temperature on trait size and growth in *Drosophila*. *Front. Cell Dev. Biol.* 6, 156.
60. Diwanji, N., and Bergmann, A. (2019). Two sides of the same coin – compensatory proliferation in regeneration and cancer. *Adv. Exp. Med. Biol.* 1167, 65–85.
61. Haynie, J.L., and Bryant, P.J. (1977). The effects of X-rays on the proliferation dynamics of cells in the imaginal wing disc of *Drosophila melanogaster*. *Wilhelm Roux Arch. Dev. Biol.* 183, 85–100.
62. Huh, J.R., Guo, M., and Hay, B.A. (2004). Compensatory proliferation induced by cell death in the *Drosophila* wing disc requires activity of the apical cell death caspase DRONC in a nonapoptotic role. *Curr. Biol.* 14, 1262–1266.
63. Pérez-Garijo, A., Shlevkov, E., and Morata, G. (2009). The role of Dpp and Wg in compensatory proliferation and in the formation of hyperplastic overgrowths caused by apoptotic cells in the *Drosophila* wing disc. *Development* 136, 1169–1177.
64. Ankawa, R., Goldberger, N., Yosefzon, Y., Koren, E., Yusupova, M., Rosner, D., Feldman, A., Baror-Sebban, S., Buganim, Y., Simon, D.J., et al. (2021). Apoptotic cells represent a dynamic stem cell niche governing proliferation and tissue regeneration. *Dev. Cell* 56, 1900–1916.e5.
65. Kawaue, T., Yow, I., Pan, Y., Le, A.P., Lou, Y., Loberas, M., Shagirov, M., Teng, X., Prost, J., Hiraiwa, T., et al. (2023). Inhomogeneous mechano-transduction defines the spatial pattern of apoptosis-induced compensatory proliferation. *Dev. Cell* 58, 267–277.e5.
66. Merino, M.M., Rhiner, C., Lopez-Gay, J.M., Buechel, D., Hauert, B., and Moreno, E. (2015). Elimination of unfit cells maintains tissue health and prolongs lifespan. *Cell* 160, 461–476.
67. Houle, D., Bolstad, G.H., van der Linde, K., and Hansen, T.F. (2017). Mutation predicts 40 million years of fly wing evolution. *Nature* 548, 447–450.
68. Herbert, S., Valon, L., Mancini, L., Dray, N., Caldarelli, P., Gros, J., Esposito, E., Shorte, S.L., Bally-Cuif, L., Aulner, N., et al. (2021). LocalZProjector and DeProj: a toolbox for local 2D projection and accurate morphometrics of large 3D microscopy images. *BMC Biol.* 19, 136.
69. Rohlf, F.J., and Slice, D. (1990). Extensions of the Procrustes method for the optimal superimposition of landmarks. *Syst. Zool.* 39, 40–59.
70. Adams, D.C., and Otárola-Castillo, E. (2013). geomorph: an r package for the collection and analysis of geometric morphometric shape data. *Methods Ecol. Evol.* 4, 393–399.
71. Chimata, A.V., Deshpande, P., Mehta, A.S., and Singh, A. (2022). Protocol to study cell death using TUNEL assay in *Drosophila* imaginal discs. *Star Protoc.* 3, 101140.
72. Classen, A.K., Aigouy, B., Giangrande, A., and Eaton, S. (2008). Imaging *Drosophila* pupal wing morphogenesis. *Methods Mol. Biol.* 420, 265–275.
73. Schindelin, J., Arganda-Carreras, I., Frise, E., Kaynig, V., Longair, M., Pietzsch, T., Preibisch, S., Rueden, C., Saalfeld, S., Schmid, B., et al. (2012). Fiji: an open-source platform for biological-image analysis. *Nat. Methods* 9, 676–682.
74. Etournay, R., Merkel, M., Popović, M., Brandl, H., Dye, N.A., Aigouy, B., Salbreux, G., Eaton, S., and Jülicher, F. (2016). TissueMiner: a multiscale analysis toolkit to quantify how cellular processes create tissue dynamics. *eLife* 5, e14334.
75. Márquez, E.J., Cabeen, R., Woods, R.P., and Houle, D. (2012). The measurement of local variation in shape. *Evol. Biol.* 39, 419–439.
76. van Kampen, N.G. (2007). Preface to the third edition. In *Stochastic Processes in Physics and Chemistry*, Third Edition (North-Holland Personal Library), p. Xi.
77. Bivand, R.S., and Wong, D.W.S. (2018). Comparing implementations of global and local indicators of spatial association. *TEST* 27, 716–748.

## STAR★METHODS

### KEY RESOURCES TABLE

REAGENT or RESOURCE	SOURCE	IDENTIFIER
<b>Antibodies</b>		
Anti E-cad concentrated (rat)	DSHB	RRID: AB_528120
Anti DSRF (mouse)	Seth Blair	N/A
Anti Delta (rat)	François Schweisguth	RRID: AB_528194
Anti GFP (chicken)	Abcam	RRID: AB_300798
Anti RFP (Rabbit)	Abcam	RRID: AB_945213
Anti cleaved DCP-1 (rabbit)	Cell signaling	RRID: AB_2721060
Anti β-gal (chicken)	Abcam	RRID: AB_307210
Anti Wingless concentrated (mouse)	DSHB	RRID: AB_528512
Anti Patched concentrated (mouse)	DSHB	RRID: AB_528441
Anti Rabbit IgG Alexa 555 (goat)	Invitrogen	RRID: AB_10374475
Anti Chicken IgY alexa 488 (goat)	Invitrogen	RRID: AB_2866499
Ultrapurified anti mouse IgG dylight 405 (donkey)	Jackson ImmunoResearch	RRID: AB_2632572
Ultrapurified anti rat IgG Cy3 (donkey)	Jackson ImmunoResearch	RRID: AB_2340667
Ultrapurified anti rat IgG Cy3 (donkey)	Jackson ImmunoResearch	RRID: AB_2315777
Ultrapurified anti rat IgG alexa 647 (donkey)	Jackson ImmunoResearch	RRID: AB_2340694
<b>Other fluorescent reagents</b>		
Phalloidin alexa 647	Invitrogen	A22287
TUNEL kit TMR red	Roche diagnostics	12156792910
<b>Experimental Models: <i>Drosophila melanogaster</i> lines</b>		
UAS-GC3Ai /TM6b	Magali Suzanne <sup>45</sup>	none
w; UAS-GC3Ai/Cyo; MKRS/TM6b	Bloomington and <sup>45</sup>	BDCS_84346
UAS-hid dsRNA	VDRC	GD 8269
UAS-lacZ	Bloomington	BDCS_8529
UAS-dronc <sup>DN</sup>	Bloomington	BDCS_58992
GMR11F02-gal4	Bloomington	BDCS_48928
w <sup>118</sup>	Bloomington	BDCS_3605
UAS-dicer2; nubbin-gal4	Bloomington	BDCS_25754
w; ; hid <sup>d.GFP</sup> /TM3	Jean-Paul Vincent <sup>47</sup>	none
yw; ET40-QF, QUAS-tdTomato; FRT82B, tub-QS	Bloomington	BDCS_30042
yw, hs-flp22, UAS-GFP; if/Cyo ; tub-gal4, FRT82B, tub-gal80/TM6b	This study and Bloomington	BDCS_86311
yw; UAS-mCd2RFP , UAS-dsRNACD8 FRT40A ; TM3/TM6b	Bloomington	BDCS_56184
yw; UAS-mcd8GFP, UAS-dsRNACD2 FRT40A ; TM3/TM6b	Bloomington	BDCS_56185
w; ptc-gal4	Bloomington	BDCS_2017
w; GMR83F09-gal4	Bloomington	BDCS_40367
w; GMR36C06-gal4	Bloomington	BDCS_49931
w; tub-gal80ts	Bloomington	BDCS_7108
w; UAS-lacZ	Bloomington	BDCS_8529
w; ; rpr-LacZ	Bloomington	BDCS_58793

(Continued on next page)

**Continued**

REAGENT or RESOURCE	SOURCE	IDENTIFIER
w; ; <i>grim-gal4</i>	Bloomington	BDCS_29117
w; ; <i>diap1-LacZ</i>	Bloomington	BDCS_12093
w; 20xUAS-EGFPx6	Bloomington	BDCS_52261
w; ; <i>Df(3L)H99 FRT80B/TM2</i>	Andrea Bergman	None
yw <i>hs-flp22</i> ; ; <i>arm-βgal FRT80B</i>	Bloomington	BDCS_6341
w; ; <i>ubi-EGFPnls FRT80B</i>	Bloomington	BDCS_5630
w; ; <i>nab-Gal4</i>	DGRC Kyoto	DGRC_104533
w; <i>UAS-miRHG</i>	Jae Park <sup>55</sup>	None
yw; <i>p(LacW)Dark<sup>CD4</sup></i>	Bloomington	BDCS_23286
w; <i>E-cad::3XmKate(KI)/Cyo GFP</i>	Yohanns Bellaïche <sup>57</sup>	None
w; <i>lexAOP-GC3Ai</i>	This study	This study
w; <i>act-lexA</i>	Bloomington	BDCS_62567
<b>Oligonucleotides</b>		
GC3AI_F: ATCCTTACTTCAGGCGGCC	This study	N/A
GCGAATTGCCACCATGTACCCCTA		
GC3AI_R: ACAAAAGATCCTCTAGACTTA	This study	N/A
CAGGTCCCTCCTCGCTGAT		
Actin42A_F:	This study	N/A
GAGCGCGGTTACAGCTTCA		
Actin42A_R:	This study	N/A
TCCTTGATGTCGCCACA		
Hid_F:	This study	N/A
GTACCAGAGCCAGCAGAGTG		
Hid_R:	This study	N/A
GCGGATGGGGATTCGAGTTC		
<b>Recombinant DNA</b>		
pCDH-puro-CMV-GC3Ai plasmid	Addgene	RRID: Addgene_78910
pJFRC19-13XLexAop2-IVS-myR::GFP plasmid	Addgene	RRID: Addgene_26224
<b>Software and algorithms</b>		
Matlab with Image processing toolbox and Statistics and Machine learning toolbox	<a href="https://fr.mathworks.com/">https://fr.mathworks.com/</a>	N/A
Fiji (ImageJ)	<a href="https://fiji.sc/">https://fiji.sc/</a>	N/A
Black Zen Software	Zeiss	RRID: SCR_01863
Mypic Zen autofocus macro	<a href="https://git.embl.de/grp-ellenberg/mypic">https://git.embl.de/grp-ellenberg/mypic</a>	N/A
MetaMorph	<a href="https://www.moleculardevices.com/">https://www.moleculardevices.com/</a>	N/A
Local z-projector plugin (Fiji)	<a href="https://gitlab.pasteur.fr/lah-public/localzprojector">https://gitlab.pasteur.fr/lah-public/localzprojector</a>	Hebert et al. <sup>58</sup>
R	<a href="https://www.r-project.org/">https://www.r-project.org/</a>	N/A
Wings4 software	<a href="https://www.bio.fsu.edu/~dhoule/wings.html">https://www.bio.fsu.edu/~dhoule/wings.html</a>	Houle et al. <sup>53</sup>
CPR 64bit	<a href="https://www.bio.fsu.edu/~dhoule/wings.html">https://www.bio.fsu.edu/~dhoule/wings.html</a>	Houle et al. <sup>53</sup>
R geomorph package	<a href="https://cran.r-project.org/web/packages/geomorph/index.html">https://cran.r-project.org/web/packages/geomorph/index.html</a>	Rohlf and Slice <sup>69</sup>
Lory	<a href="https://www.bio.fsu.edu/~dhoule/lory.html">https://www.bio.fsu.edu/~dhoule/lory.html</a>	Adams and Otárola-Castillo <sup>70</sup>
<b>Raw data and codes</b>		
Raw data	<a href="https://doi.org/10.5281/zenodo.10261295">https://doi.org/10.5281/zenodo.10261295</a>	This manuscript
Original codes	<a href="https://doi.org/10.5281/zenodo.10276156">https://doi.org/10.5281/zenodo.10276156</a>	This manuscript

**RESOURCE AVAILABILITY**

**Lead contact**

Further information and requests for resources and reagents should be directed to and will be fulfilled by the lead contact, Romain Levayer ([romain.levayer@pasteur.fr](mailto:romain.levayer@pasteur.fr)).

### Materials availability

All the reagents and strains generated in this study will be shared upon request to the lead contact without any restriction.

### Data and code availability

- All raw data corresponding to each figure panel (including images and local projection) have been deposited in a single Zenodo repository (<https://doi.org/10.5281/zenodo.10261295>) and are publicly available as of the date of publication. The DOI is also listed in the [key resources table](#).
- All original code has been deposited in a Zenodo repository (<https://doi.org/10.5281/zenodo.10276156>) and is publicly available as of the date of publication. The DOI is also listed in the [key resources table](#).
- Any additional information required to reanalyse the data reported in this paper is available from the [lead contact](#) upon request.

## EXPERIMENTAL MODEL AND SUBJECT DETAILS

### Drosophila melanogaster husbandry

All the experiments were performed using *Drosophila melanogaster* fly lines (listed in the [key resources table](#)) breed with regular husbandry techniques. The fly food used contains agar (7.6 g/l), saccharose (53 g/l) dry yeast (48 g/l), maize flour (38.4 g/l), propionic acid (3.8 ml/l), Nipagin 10% (23.9 ml/l) all mixed in one liter of distilled water. Flies were raised at 25°C in plastic vials with a 12h/12h dark light cycle at 60% of moisture unless specified in the legends and in the [Table S1](#) (alternatively raised at 18°C or 29°C).

### Drosophila melanogaster strains

The strains used in this study and their origin are listed in the [key resources table](#). Females and males were used without distinction for all the experiments, except for the adult wing shape analysis in which only left wings from female flies were used. We did not determine the health/immune status of pupae, adults, embryos and larvae, they were not involved in previous procedures, and they were all drug and test naïve. The exact genotype used for each experiment is listed in the [Table S1](#).

## METHOD DETAILS

### Design of lexAOP-GC3Ai fly line

p13xLexAop2-GC3Ai was generated by PCR-amplifying GC3Ai from pCDH-puro-CMV-GC3Ai (Addgene 78910) and cloned in pJFRC19-13XLexAop2-IVS-myr::GFP (Addgene 26224) cut with NotI and XbaI (to excise myr::GFP) and inserted using In-Fusion assembly method. The construct was checked by sequencing and inserted at the attP site attP40A after injection by Bestgene.

The following primers were used for GC3Ai amplification:

GC3AI\_F: ATCCTTACTTCAGCGGCCGAAATTGCCACCATGTACCCCTA

GC3AI\_R: ACAAAAGATCCTCTAGACTTACAGGTCCCTCGCTGAT

### QPCR validation of Hid depletion

Hid depletion by RNAi and microRNA was validated by RTPCR. Total RNA was prepared from wing imaginal disc expressing hid-dsRNA or mirRHG under the control of the Nab-Ga4 driver (non-Tb larvae) using TRIzol reagent (Invitrogen). RNA (1ug) was retrotranscribed using random primers and Superscript III reverse transcriptase (Invitrogen). cDNA was analyzed by qPCR using FastStart Universal SYBR Green (Roche) and Actin-42A was used as a reference gene. The primers used for Actin 42A and Hid amplifications were the following:

Actin 42A\_F: GAGCGCGGTTACAGCTTCA

Actin 42A\_R: TCCTTGATGTCGCGCACA

Hid\_F: GTACCAGAGCCAGCAGAGTG

Hid\_R: GCGGATGGGGATTGAGTC

All assays were performed in triplicate, and mean values were calculated according to the ΔCT quantification method. Results are expressed as the average from at least three independent experiments normalised to the control condition (Nab-Ga4, UAS-lacZ). Doing so, we obtained an average Hid mRNA level at 0.59 for mirRHG versus 0.46 for hid dsRNA (p=0.02), suggesting a very efficient depletion in both cases, but more efficient for hid dsRNA.

### Immunostaining

Dissections of larval wing imaginal discs were performed on PBS in ice. Dissected discs were fixed for 20 min in 4 % formaldehyde (SIGMA F8775), rinsed 3 times in PBT (PBS 0.4 % Triton), followed by 10 min permeabilisation in PBT. Primary and secondary antibodies were incubated for 2 h at room temperature (or 12 h at 4 °C) under rocking agitation. After each antibody incubation, discs were rinsed 3 times in PBT, followed by 3 washes of 30 min. Discs were mounted in Vectashield® (EUROBIO SCIENTIFIC / H-1000) and imaged using a confocal spinning disc microscope (Gataca systems) with a 40X oil objective or a LSM880 equipped with a fast Airyscan using a 40X oil objective. The following primary antibodies were used: rat anti E-cadherin (1/100, DCAD2 concentrated

DSHB), mouse anti DSRF (1/500, gift of Seth Blair), rat anti Delta (1/1000, gift of François Schweiguth), chicken anti GFP (1/1000, abcam ab13970), rabbit anti RFP (1/500, abcam 62341), rabbit anti DCP-1 (1/100, Cell Signaling 9578S), chicken anti Beta-gal (1/1000, Abcam ab 9361), mouse anti Wingless (1/250, 4D4 concentrated DSHB), mouse anti Patched (1/250, Apa-1 concentrated, DSHB), phalloidin alexa 647 (1/50, Invitrogen). Secondary antibodies were: anti rabbit alexa 555 (1/500, Invitrogen), anti chicken alexa 488 (1/500, Invitrogen), ultrapurified anti mouse 405 (1/500, Jackson ImmunoResearch / 715-476-151), ultrapurified anti mouse Cy3 (1/500, Jackson ImmunoResearch / 715-165-151), ultrapurified anti rat Cy3 (1/500, Jackson ImmunoResearch / 712-165-153), ultrapurified anti rat alexa 647 (1/500, Jackson ImmunoResearch / 712-605-153). TUNEL assays for the detection of dying cells with fragmented DNA were conducted using the *In Situ Cell Death Detection Kit, TMR red* (Roche diagnostics®) and the *TUNEL dilution buffer* (Roche diagnostics®), following the experimental procedure described in Chimata et al.<sup>71</sup>

### Live imaging of pupal wing

Pupa were collected at early fluid stage and kept at 29°C for 7 h, resulting in pupa aged of ~15 h APF (after pupal formation). Pupal wings were prepared for live imaging as described in Classen et al.<sup>72</sup> Briefly, pupa were glued on their lateral side on a support made of three layers of tape (one layer of single-side tape, a second layer of double-side tape, and a third layer of single-side tape), and a window was opened using a pair of fine scissors (Fine Science Tools) in the pupal case to expose the pupal wing tissue. The wing was covered with halocarbon 10S oil, and the tape with the pupa on it was mounted on a glass bottom dish of 1,5 µm thickness (Miltenyi Biotec). Imaging was done on a confocal spinning disc microscope (Gataca systems, Metamorph software) with a multi-immersion 20X objective with oil (N.A. 0.75). The dorsal epithelial layer of the wing was scanned on a mosaic of two (x,y) tiles, and Z-stacks of 50 µm (20 slices of 2.5 µm), every 15 min at room temperature (~22 °C). Z projections were done using the Fiji LocalZProjector using E-cad plane as a reference<sup>68</sup>

### QUANTIFICATION AND STATISTICAL ANALYSIS

#### Image processing

All images were processed using FIJI.<sup>73</sup> For the twin clones analyses, Z projections of z-stacks were done using the Fiji LocalZProjector plugin using E-cad or phalloidin staining as a reference plane,<sup>68</sup> allowing to project a limited number of planes around the apical junction plane while following the local disc curvature. *hid*<sup>ΔGFP</sup> pattern measurements were done after fixation and GFP immunostaining and maximum z projection. The mean GFP intensity was measured in each compartment (defined with DSRF staining) and normalised by the mean GFP intensity of the full wing pouch.

#### QMRCM and mitotic clones experiments

Wandering larvae were collected 48 hours after clone induction following a 37°C heat-shock of 8 or 10 minutes (Table S1). Analysis of twin clones was performed on local projections of the wing discs after fixation and staining. Only discs with sufficiently sparse distribution of clones were used (to assign twins unambiguously). To extract clone position and size, each mitotic recombination figure (twin spot or single clone) was manually outlined on FIJI and then automatically segmented by applying a Gaussian blur followed by an automated thresholding (Intermode white method). The centroid of each mitotic recombination figure was obtained by summing the centres of each individual patch of cells composing the twin spot, ponderated by their relative area compared to the total area of the twin clone. Thus, the centroid of each mitotic recombination figure was given by the following formula:

$$\text{Centroid } (x, y)_{\text{mitotic figure}} = \sum_{\text{clone } i} (\text{Centroid } (x, y)_{\text{patch } i}) \cdot \frac{\text{Area}_{\text{patch } i}}{\text{Total Area twin clone}}$$

Averaged clone surface was estimated through the segmented surface of GFP or RFP clones (using the local projection around the apical plane of cells). Estimation of the clone size in cell number was obtained a posteriori by segmenting (using Tissue analyser<sup>74</sup>) 3 wing discs stained with E-cad (Figure S3A) and DSRF to position landmarks, and by estimating the averaged apical cell area for each compartment. The 3 wing discs segmented for apical cell area shown a very congruent pattern thus allowing to pool the data from the 3 discs (Figure S3B). The average surface of clone for each compartment was then divided by the local averaged cell size to obtain an estimation of cell number per clone and to correct for effects driven by inhomogeneity of cell apical size throughout the disc.

For mitotic clones (H99 and WT sibling clones, ubi-GFP and arm-β-gal WT neutral mitotic clones), E-cad and phalloidin signals were used to project locally the β-gal signal (the absence of LacZ marking the H99 allele) using the local z-projection Fiji plugin<sup>68</sup> and combined with DSRF staining. The same procedure was applied to GFP and β-gal for neutral mitotic clones, except that the projection was performed around the nucleus plane. A 3D gaussian blur filter was applied on the β-gal and GFP signal (1px width in X,Y,Z). For H99 mitotic clones, homozygous mutant (no β-gal signal) and WT siblings (2 copies of β-gal) were recognised manually, and their contours drawn by hands on Fiji. The same procedure was applied to neutral mitotic clones (comparing clones with 2 copies of β-gal without GFP, and clones with two copies of GFP without β-gal). We only used discs with sufficiently sparse clones and proper β-gal/GFP signal and counted single clone only when there was no ambiguity. Twin clone localisation was then assigned using the centroid estimation described above.

**Spatial maps of wing discs (twin clones and GC3Ai)**

Positions of 36 landmarks were manually set on Z projections of wing discs using FIJI. Landmarks were positioned according to the pattern of DSRF revealed by immunostaining, along the veins, margin and folds of the wing pouch (Figures S1A and S1B). Two methods were used to characterise a spatial map of the tissue based on landmarks position. For the first one, landmarks were geometrically aligned within each genotype using the General Procrustes Analysis (GPA)<sup>69</sup> as implemented in R geomorph package.<sup>70</sup> GPA translates the set of landmarks of each wing disc to the same origin, scales them to size, and rotates them until the coordinates of corresponding points align as closely as possible. GPA allows to superimpose as closely as possible several wing discs, thus allowing superimposition of the signal from many individuals (Figures 1F, S1H, S1J, S1M, S1P, and S1R). For the second mapping method, 14 additional landmarks were added (landmarks 37 to 50) at the centre of segments defined by other landmarks (for example landmark 37 was set as the centre of the segment defined by landmarks 21 and 22, Figure S1C). The resulting 50 landmarks were thus used to define polygons dividing the wing disc tissue into 40 compartments (Figure S1C). With this later approach, clones and apoptotic bodies (defined by GC3Ai or cleaved DCP-1 figures) were assigned to a compartment according to the coordinates of the centre of mass of the clone/apoptotic body. In order to account for uncertainty in clone/apoptotic body localisation (e.g., because of clone movement between the time of induction and imaging), as well as for uncertainty in landmark positioning (e.g., because of immunostaining variability or user error), clone assignment included consideration of an error margin. We used the *st\_buffer* function implemented in the *sf* package of R software to add an error margin at a distance of 11.8 µm (40 pixels) around compartment margins (Figure S1D). As a result, buffered boundaries of neighbour compartments overlap within each other and a given position in the tissue could be assigned to belong to more than one compartment. This results in a smoothing of the spatial map allowing to account for uncertainty in cells and landmarks positions.

To analyse the spatial pattern of GC3Ai in discs at 72 h AEL, the anti DSRF staining could not be used to draw the landmarks because at this stage the DSRF patterning is not yet established. Instead we stained the wing discs for Ptc and Wg to detect AP and DV compartment and subdivide the wing disc in 4 quadrants (Anterior-Dorsal; Anterior-Ventral; Posterior-Dorsal; Posterior-Ventral).

**Adult wing shape and size analyses**

Crosses were done by placing 50-100 couples in egg laying cages with juice-agar plates kept at 25 °C. Freshly hatched larva from the agar plates were transferred to *Drosophila* vials with fly food as described above at a density of 30 individuals / vial, and grown at 18 °C, 25 °C or 29 °C until emergence of adults. Flies were collected and stored in ethanol 70 % at room temperature until dissection. Only left wings from females were taken, and mounted dorsal side up on a glass slide in a solution of 1:1 ethanol 80% and lactic acid 90%. Imaging was carried out on a ZEISS Discovery V8 stereomicroscope using a ZEISS Axiocam ICc 5 camera. All wings were imaged in the same orientation and with the same imaging parameters. For the experiments using Gal80ts (Figures 5, S4, and S5), flies were crossed in cages supplied with agar petri dishes and allowed to lay eggs for 6 to 12 h. Freshly hatched larva were transferred to regular vials at a density of 30 individuals / tube, and placed at 18 °C or 29 °C. Once arrived at the wandering larval stage, individuals where switched temperature (from 18 °C to 29 °C and vice-versa). Upon hatching, flies were collected for wing dissection.

Wing measurements were done using a semi-automated procedure for estimating the positions of 12 landmarks and 37 semi-landmarks along the wing outline and veins (Figure S4A). This was done using Wings4 software<sup>53,54</sup> which fits a B-spline model to the wing from which the coordinates of landmarks and semi-landmarks are extracted. Wings4 outputs were examined using CPR software<sup>54</sup> which allows to screen for outliers and to generate a consolidated dataset of landmarks and wing areas.

Landmarks data were geometrically aligned within each experiment using the General Procrustes Analysis (GPA)<sup>69</sup> as implemented in R geomorph package.<sup>70</sup> GPA translates all wing images to the same origin, scales them to unit-centroid size (centroid size is a measure of specimen size computed as the square root of the sum of squared distances of all the landmarks from the specimen's centroid) and rotates them until the coordinates of corresponding points align as closely as possible. Differences in landmarks coordinates resulting from the GPA represent shape differences between wings. Wing shape of each individual is characterised by the value of 96 variables, coming from the Procrustes transformation of x and y coordinates of the 48 landmarks and semi-landmarks. To reduce dimensionality of the data, wing shape variation was analysed by Principal Components Analysis as implemented in the function *plotTangentSpace* (now deprecated and replaced by *gm.prcomp*) of the R *geomorph* package. Visualisation of the wing shape variation among the principal component axes was done by comparing wing shape of the individual presenting the lowest value along the axis, with the individual presenting the highest value. To enable visualisation of local growth differences in the adult wing upon apoptosis inhibition, we used the program Lory<sup>75</sup> to show one pattern of relative expansion or contraction that can transform mean shape of control genotype into mean shape of genotypes where apoptosis was inhibited.

**Estimation of clone size differences in an exponential growth regime**

The aim of this analysis is to predict spatial differences of clone size under an exponential growth regime given the estimated spatial differences of apoptosis rate based on the twin-clone experimental assays. For the sake of simplicity, we assume that division rate and apoptosis rate are constant over time.

**Estimation of the clone extinction probability**

Upon recombination, two daughter cells of different colours are generated and continue to grow, divide and die. After a given time *T* (time of observation), there are four possible outcomes: we can recover the two daughter clones, a single colour clone, green or red

(the other clone died before time  $T$ ), and finally both clones disappeared before time  $T$  (which cannot be measured experimentally). For this estimation, we assumed that both lineages (green and red) have the same proliferation and death rates.

$n(t)$  is the size (number of cells) of a clone at the time  $t$ , and is a stochastic process that follows the same probability function for every clone. For every clone, we have  $n(0) = 1$ . The probability of clone disappearance before time  $t$ . i.e. the extinction probability,  $p_0(t)$  is defined as

$$p_0(t) = P(n(t) = 0).$$

Experimental data gives access to the number of single clones  $N_s$  and to the number of twin clones  $N_d$  that we observe at the time  $T$ . From this, we can estimate the probability of extinction at the observation time  $T$ ,  $p_0 = p_0(T)$ .

The expected number of single clones is  $N_s = 2p_0(1 - p_0)$

The expected number of twin clones is  $N_d = (1 - p_0)^2$  which gives the estimator of  $p_0$ ,

$$\hat{p}_0 = \frac{q}{2 - q} \quad (\text{Equation 1})$$

$$\text{where } q = \frac{N_s}{N_s + N_d}$$

### Estimation of the clone size and relationship with apoptosis and proliferation rate

Let  $\mu(t)$  be mean value of  $n(t)$ , clone size in number of cell at time  $t$ . In theory:

$$\mu(t) = p_0(t) \cdot 0 + p_1(t) \cdot 1 + \dots + p_i(t) \cdot i + \dots,$$

where  $p_i(t)$  is a probability to observe a clone of size  $i$  at the given time  $t$ , or  $p_i(t) = P(n(t) = i)$  and  $\sum p_i(t) = 1$  for all  $t$ . In order to estimate  $\mu(t)$  from the observations we use:

$$\hat{\mu} = \frac{k_0}{N} \cdot 0 + \frac{k_1}{N} \cdot 1 + \dots + \frac{k_i}{N} \cdot i + \dots,$$

where  $N$  is a total number of clones (including clones of size "0"),  $k_i$  is a number of clones of size  $i$ , and  $\sum k_i = N$ .

However, since we cannot observe clones of size 0 we cannot measure  $k_0$  nor  $N$ . We therefore use  $p_0 = \frac{k_0}{N}$  (the probability of clone extinction, see above), and the total number of observed clones  $N_{obs} = N - k_0$ . From these two we can estimate  $N = \frac{N_{obs}}{1 - p_0}$ . Hence, we estimate  $\mu$  with

$$\hat{\mu} = (1 - \hat{p}_0) \left( \frac{k_1}{N_{obs}} \cdot 1 + \dots + \frac{k_i}{N_{obs}} \cdot i + \dots \right). \quad (\text{Equation 2})$$

Each clone observed is a result of a stochastic birth-death process, that is fully described by its death rate,  $a$ , which is a probability of an individual cell to die per unit time and its birth rate,  $b$ , which is a probability of an individual cell to divide per unit time. While the size of the clone at the given time,  $n(t)$ , is a stochastic process, the mean size  $\mu(t)$  can be approximated by a deterministic process and is given by the following exponential function:

$$\mu(t) = e^{(b-a)t} \quad (\text{Equation 3})$$

Furthermore, the probability to be extinct at the time  $t$  ( $n(t) = 0$ ) can be expressed as follows<sup>76</sup>:

$$p_0(t) = \frac{a - ae^{-(b-a)t}}{b - ae^{-(b-a)t}} \quad (\text{Equation 4})$$

### Estimating the apoptosis and proliferation rates for each compartment

From the twin clone experimental data, we retrieve for each compartment the proportion of single clone occurrence (Figure 2C) and the averaged clone size (Figure 3A) which, together with (Equation 1), allows us to estimate  $p_0$ , and  $\mu$  for each of the 40 compartments of the wing disc. These estimates can then be used to estimate parameters  $a$  and  $b$  (apoptosis and division rate). For the fixed  $t$ , based on (Equation 3) and (Equation 4) we have:

$$b = \frac{\ln(\mu)}{t} + a \quad (\text{Equation 5})$$

and

$$p_0 = \frac{a - \frac{a}{\mu}}{b - \frac{a}{\mu}} \quad (\text{Equation 6})$$

Hence

$$a = \frac{\ln(\mu)}{t \left[ \frac{1}{\mu} + \frac{\mu - 1}{\mu p_0} - 1 \right]} \quad (\text{Equation 7})$$

#### Estimating the expected differences of clone size between compartments assuming constant proliferation rate

We use the fixed value of a birth rate,  $b = 0.0657$  (average of the estimated  $b$  from (Equation 5)), as a fixed value for every compartment. We look for a death rates  $a$  for each compartment using the expression for  $p_0(a)$  (Equation 4). To the best of our knowledge it is not possible to express explicitly  $a$  from the given formulation, so we use numerical approach to calculate it. We plot function of  $p_0$  as  $p_0(a)$  and look for the point of intersection with the measured value  $\hat{p}_0$ . In this way we estimate value of  $a$ . Then we use  $a$  and the fixed value of  $b$  to predict  $\mu$  (Equation 6), that we then compared with the estimated value  $\hat{\mu}$  from the experimental data (Equation 2) correcting for the non-observable disappeared clones (see Figure 3B). We overall found a good correlation between the estimated clone size and the prediction, (correlation coefficient = 0.6, Figure 3D) suggesting that the spatial differences in apoptosis are to a good approximation sufficient to explain the spatial differences in average clone size.

#### Statistical analysis

Data were not analysed blindly. No specific method was used to predetermine the number of samples. The definition of  $n$  and the number of samples is given in each figure and associated legend. Error bars are standard error of the mean (s.e.m.) or confidence interval 95%. Test for spatial autocorrelations in apoptosis patterns were conducted using Moran's statistics implemented in the *moran.mc* function from the *spdep* R package.<sup>77</sup> This tests for spatial clustering of apoptosis levels, by testing the hypothesis that the levels of apoptosis are randomly distributed across the 40 compartments, versus the hypothesis that the level of apoptosis of a given compartment is correlated with the levels of the neighbouring compartments. Tests for spatial correlation across compartments between log transformed GC3Ai levels and % of single clones occurrences were done using the function *wtd.cor* from *weights* R package (v. 1.0.4), which produces a Pearson's correlation test and uses weights for calculation of the correlations. In this case, we weighted the values for the % of single clones by the number of mitotic events over which the percentage was estimated within each compartment, thus giving higher weights to the compartments for which percentages were estimated over a large number of events. Bootstrapping analysis was used to assess the distribution of differences between Hid-dsRNA and LacZ adult wing size at different temperatures upon larval and pupal induction at 29°C (Figure 5A). 50 random resamplings of each dataset was performed and used to look at the percentage of variation of the difference obtained for each condition between the lacZ and Hid-dsRNA flies. We then assessed the overlap of the distribution and confirmed that the difference between LacZ and Hid-dsRNA at 18° (control) is similar to the difference between LacZ and Hid-dsRNA induction during pupal stage (18°C–29°C), while the differences were higher than the control for all the other conditions.